Dynamically Induced Displacements of a Persistent Cold-Air Pool

Neil P. Lareau and John D. Horel

Neil Lareau
Department of Atmospheric Sciences, University of Utah, 135 S 1460 E Room 819 WBB, Salt Lake City, UT, 84112-0110, USA
Email: neil.lareau@utah.edu; Phone: 860-716-0417

John Horel
Department of Atmospheric Sciences, University of Utah, 135 S 1460 E Room 819 WBB, Salt Lake City, UT, 84112-0110, USA

Abstract This study examines the influence of a passing weather system on a persistent cold-air pool (CAP) during the Persistent Cold-Air Pool Study in the Salt Lake Valley, UT. The CAP experiences a sequence of along-valley displacements that temporarily and partially remove the cold air in response to increasing along-valley winds aloft. The displacements are due to the formation of a mountain wave over the upstream topography as well as adjustments to the regional pressure gradient and wind stress acting on the CAP. These processes appear to help establish a balance wherein the depth of the CAP increases to the north. When that balance is disrupted, the CAP depth collapses, which sends a gravity current of cold air back upstream and thereby restores CAP conditions throughout the valley. Intra-valley mixing of momentum, heat, and pollution within the CAP by Kelvin-Helmholtz waves and seiching is also examined.

Keywords Cold-air Pool, Inversion, Kelvin-Helmholtz Instability, Mountain Wave Turbulent Mixing, Seiche, Stable Boundary Layer

1 Introduction

The disruption of persistent cold-air pools (CAPs) arising from passing weather systems is examined in this study. CAPs are decoupled air masses that form in mountain valleys and basins due to cooling of the air near the surface, warming of the air aloft, or both (Whiteman et al. 1999). The resulting stable stratification suppresses vertical mixing while the confining topography prevents advection and favors air stagnation. Persistent CAPs are simply CAPs surviving through more than one diurnal cycle (Whiteman et al. 2001).

Persistent CAPs are often accompanied by adverse societal impacts. When they occur in densely settled valleys, the emissions from vehicles, home heating, and industrial sources accumulate, leading to unhealthy air quality (Reddy et al. 1995; Pataki et al. 2005; Pataki et al. 2006; Malek et al. 2006; Silcox et al. 2012). High particulate concentrations during CAPs have recently been linked to increased risk for cardiovascular disease and asthma and may lead to decreased lifespan (Pope et al. 2009; Beard et al. 2012). Suppressed temperatures within CAPs combined with the presence of snow cover can also increase the likelihood of fog, which affects air and ground transportation (Wolyn and Mckee 1989).

The strength and longevity of persistent CAPs is modulated by the synoptic conditions establishing them, the surface energy budget, and subsequent interactions with passing weather systems (Wolyn and Mckee 1989; Whiteman et al. 1999; Whiteman et al. 2001; Reeves and Stensrud 2009; Gillies et al. 2010; Chow et al. 2013). CAPs most often form during the warming aloft accompanying the arrival of high-pressure weather systems. Weak disturbances may then temporarily perturb a CAP, whereas more vigorous baroclinic troughs are likely to completely destroy them, especially those accompanied by strong cold-air advection (Whiteman et al. 1999; Whiteman et al. 2001; Zhong et al 2001; Reeves and Stensrud 2009; Chow et al 2013).

In the absence of strong cold-air advection, forecasting the demise of CAPs remains a challenge. During such situations, CAP removal may be controlled by interactions among four other mechanisms: (1) internal *convection*, (2) top-down *turbulent erosion*,(3) CAP *displacement* and (4) *airflow* over the upstream topography (Lee et al. 1989; Petkovšek 1992; Petkovšek and Vrhovec 1994; Gubser and Richner 2001; Zängl 2003; Zängl 2005; Flamant et al. 2006).

In contrast to diurnal CAPs that form overnight and are destroyed by daytime heating, *convection* alone is generally insufficient to destroy persistent CAPs due to weak sensible heat flux during the winter (Zhong et al. 2001). However, when other processes are weakening a CAP, convection may become an important factor in breakup (Whiteman et al. 1999; Zhong et al. 2001, Chow et al. 2013). For example, Whiteman et al. (1999) show that the final removal of persistent CAPs preferentially occurs in the afternoon when sensible heat flux is strongest.

The second mechanism, *turbulent erosion*, is the break down of CAP stratification via irreversible turbulent motions. Petkovšek (1992) proposed a semi-analytic model for this process wherein turbulent flow above a CAP progressively erodes downward into the stratified air. In this scenario, the CAP thins, but also strengthens, in time. The strengthened CAP subsequently suppresses the rate of turbulent encroachment, thus requiring an accelerating wind aloft for erosion to continue. Zhong et al. (2003) diagnose the time-scale for turbulent CAP erosion using idealized CAP profiles and steady winds at different strengths. Their results show that the erosion rate decays in time, consistent with Petkovšek's hypothesis, and that turbulent erosion is very slow for typical CAP scales and thus unlikely to cause CAP breakup independent of other processes.

Turbulent erosion of stratification has also been observed in other geophysical flows, such as mixing across the thermocline in lakes and oceans (Fernando 1991). Strang and Fernando (2001 a, b) use laboratory tank experiments to examine the deepening rate of a mixed layer into a stable layer and show that mixed layer deepening progresses via Kelvin-Helmholtz and other dynamic instabilities, the occurrence of which is controlled by the Richardson number.

CAP *displacement*, the third process, is the rearrangement of CAP mass via static and dynamic processes. Petkovšek and Vrhovec (1994), and later Zängl (2003), show that CAPs hydrostatically adjust to regional pressure gradients by developing a sloping interface and thus an internal pressure gradient that offsets the pressure gradient aloft. When the CAP slope becomes sufficiently large, cold-air spills over the confining topography and the volume of air within CAP is reduced (Zängl 2003). CAP tilt may also have a component due to wind stress acting on the CAP (Petkovšek and Vrhovec 1994, Gubser and Richner 2001, Zängl 2003). This effect can be particularly pronounced when winds are ageostrophic, e.g. acting in the same sense as the pressure gradient (Zängl 2003). This wind-stress effect is similar to "wind set-up" or storm surge that displaces water along the downwind fetch within lakes.

CAP displacement may also occur due to *airflow* over the upstream topography. Lee et al. (1989) examine the interaction of a mountain wave with a lee-side CAP in idealized simulations, and show that the CAP is displaced by the mountain wave unless there is an adverse pressure gradient generating an opposing surface flow toward the mountain. Interestingly, they also found that turbulent erosion was a minimal factor in CAP evolution despite strong shear.

More generally, the ventilation of valleys containing stratified air masses has been related to the Froude number (or its inverse, the non-dimensional valley depth):

$$Fr = \frac{U}{NH} \tag{1}$$

where U is the mean wind above the valley, N is the Brunt–Väisälä frequency, and H is the valley depth (Bell and Thompson, 1980; Tampieri and Hunt, 1985; Lee et al. 1987). Bell and Thompson (1980) found that when $Fr \geq 1.2$, the flow tends to sweep through a valley despite the stratification. Other studies have shown that, in addition to Fr, the terrain geometry, including ridge spacing, slope angle, and the wavelength of lee waves all affect the character of the flow into the valley (Tampieri and Hunt, 1985; Lee et al. 1987).

Relatively few observational studies have focused on the breakup of CAPs. Whiteman et al. (2001) document the differing destructive processes during two CAPs in the Columbia River Basin, one being affected by strong down slope winds and the other by cold-air advection and internal convection. Rakovec et al. (2002) examined turbulent processes during the breakup of CAPs in a Slovenian mountain valley. Using field observations and numerical experiments, they show that turbulent erosion commences above a threshold wind speed and continues if the flow accelerates. Flamant et al. (2006) examined the interaction of foehn winds with a CAP in the Rhine Valley during the Mesoscale Alpine Project. They conclude that CAP displacement along the valley axis is primarily caused by advection within the foehn flow, but also show that Kelvin-Helmholtz and gravity waves affect the CAP to a lesser degree.

In this study, we use data collected in the Salt Lake Valley of northern Utah during the Persistent Cold-Air Pool Study (PCAPS, Lareau et al. 2013) to examine the passage of a short wave trough during a multi-day CAP. This trough-CAP interaction produced a variety of waves, displacement and fronts that disrupted the otherwise quiescent CAP. In the following sections we analyze the observed changes in CAP structure and develop a simple conceptual model for the trough-CAP interaction based on the observations and an idealized numerical simulation using a Large-Eddy Simulation version of the Weather Research and Forecasting (WRF-LES) model (Skamarock et al. 2008).

2 The Salt Lake Valley and Meteorological Data

2.1 The Salt Lake Valley

The Salt Lake Valley (SLV) is located in northern Utah, USA at the eastern edge of the semi-arid intermountain west, which is the region between the Sierra Nevada and Rocky Mountains. CAPs are common in the SLV during winter, affecting the nearly 1 million residents. The meridionally-oriented valley is confined to the east and west by the Wasatch (~2800 m) and Oquirrh (~2400 m) Mountains, respectively (Fig. 1). To the south, the Traverse Mountains (~1800 m), which have ~500 m of relief, act as a partial barrier separating the SLV from the neighboring Utah Valley. The SLV opens to the northwest into the Great Salt Lake Basin. The lowest elevations in the SLV are found along the Jordan River, which slopes downward from ~1400 m as it enters the SLV through the Jordan Narrows, a gap through the Traverse Mountains, to ~1280 m at the shore of the Great Salt Lake. East-west asymmetries in the SLV have large impacts during CAPs: (1) there is more landmass at a given elevation to the west of the Jordan River, and (2) north-south flow is blocked more to the east of the River than to its west.

2.2 Meteorological Data

The meteorological data used in this study were collected during the PCAPS Intensive Observing Period 1 (IOP-1). IOP-1 examined a multi-day CAP that formed on 1 December and lasted through late on 6 December 2010. We describe here the key observational resources that are used in this study, the locations of which are shown in Fig. 1. An overview of PCAPS and all available data resources are provided by Lareau et al. (2013).

To diagnose the evolution of the IOP-1 CAP, we construct time-height profiles of temperature, potential temperature, relative humidity, and wind intended to be representative of the conditions within the central core of the SLV. For this purpose, we rely most heavily on the data collected at the Integrated Sounding System (ISS) sites labeled by blue dots in Fig. 1, which are on bluffs immediately to the west of the Jordan River. A 915 MHz radar wind profiler (RWP) and Radio Acoustic Sounding System (RASS) were operated continuously at ISS-N, while radiosondes were launched at 3-12 h intervals from ISS-S, ~1 km to the south, depending on the operational plan for the field program. We constrain these vertical profiles near the surface by automated weather observations at ISS-S and also use radiosonde data from the Salt Lake International Airport (KSLC; black dot in Fig. 1) above the boundary layer to improve the temporal coverage for periods when sondes were not launched at ISS-S. Gaps in the remote sensor data due to low signal-to-noise ratios are filled objectively using an "inpainting" analysis technique (Schönlieb 2012) and bounded by surface and radiosonde data at the gap boundaries The resulting time-height profiles are quality controlled to remove spurious unphysical values and gradients and then averaged linearly with interpolated time-height profiles from the radiosonde data alone. The final set of time-height profiles reflect an effective blend of the remote sensor and in situ observations at a temporal interval of 30 minutes and a vertical resolution of ~50 m. These profiles are representative of the conditions throughout most of the SLV during this CAP except during the Disturbance Phase, described later, when these profiles reflect conditions near the ISS sites only.

A laser ceilometer located at ISS-S is used to characterize the mixing depth of aerosol, the presence of hydrometeors, and fine-scale structures within the boundary layer at 16 s temporal resolution (Young 2013). Two pseudo-vertical transects along the confining topography are created based on lines of near-surface sensors running up the sidewalls. The first transect is composed of 6 automatic weather stations ascending the Traverse Mountains in the southeast corner of the valley (yellow dots in Fig. 1 with SM6 located on the valley floor at an elevation of 1370 m while SM1 is on the Traverse Mountain ridgeline at an elevation of 1930 m). These stations were equipped with wind, temperature, humidity and pressure sensors and recorded data every 5 minutes. The second transect uses HOBO™ temperature data loggers aligned along Harker's Ridge, which is a sub-ridge along the east slope of the Oquirrh Mountains (northern string of green dots in Fig. 1). The HOBOs also report temperature every 5 minutes and are spaced vertically at ~50 m intervals from 1350 to 2500 m.

Data from over fifty surface weather stations within the SLV with diverse suites of sensors are used from the Mesowest archive (Horel et al. 2002). In addition, seven 10-m Integrated Surface Flux System (ISFS) stations providing radiation, kinematic flux, and ground probe sensors as well as standard weather variables were deployed around the Salt Lake Valley as part of PCAPS (numbered in purple dots in Fig. 1).

3 Results

3.1 IOP-1 Overview

Wei et al. (2013) describe the conditions from 30 November – to 7 December 2010 that encompass IOP-1 without relying on the PCAPS field campaign data, i.e., they examined KSLC radiosonde and Mesowest surface observations in combination with a WRF model simulation. Based on all the PCAPS data now available, we show that the IOP-1 CAP progressed through 4 stages in its life cycle: formation, disturbance, persistence, and break-up (Fig. 2). This paper primarily examines the disturbance phase, but here we briefly summarize the event in its entirety.

3.1.1 Formation

The IOP-1 CAP followed the passage of a strong shortwave trough, which brought snow and cold temperatures to the SLV. The CAP was then initiated by mid-tropospheric ridging and warming, which formed a capping layer of strong static stability that decoupled the cold valley atmosphere from the flow above crest level (Wei et al. 2013).

The strength of the nascent CAP was subsequently augmented by a surface based radiation inversion forming during clear skies overnight on 2 December (see Fig. 2a, b). Averaged over the seven ISFS stations, the net radiative cooling in the valley on that night is the strongest during the CAP episode (Fig. 2a). Combined, the warming aloft and cooling at the surface yielded a ~700 m deep CAP with a surface potential temperature deficit (relative to that near the top of the CAP) in excess of 15 K at 12 UTC 2 December. Weak winter insolation, high albedo due to snow cover, and the strong stability suppressed the growth of the convective boundary layer the following afternoon, which allowed the CAP to persist and for aerosol to accumulate rapidly (Fig. 2b). Concentrations of small particulates surpassed the National Ambient Air Quality Standard (U.S. EPA 2013) of 35-μg m^{-3} after just the second day of the cold pool (Fig. 2c).

3.1.2 Disturbance

The disturbance phase of IOP-1 occurred on 3 December as the initial ridge broke down and a weak shortwave trough accompanied with mid-level clouds moved across the Intermountain West (Fig 3). The approaching trough generated a compact regional pressure gradient that accelerated southerly winds above the CAP, reaching a peak approaching ~20 m s^{-1} during the early morning of 3 December (Fig. 4). Terrain channeling controlled the orientation of the flow in the SLV, leading to ageostrophic south winds blowing along the valley axis and down the regional pressure gradient (not shown).

As the winds increased aloft, the CAP thinned from ~700 m at 00 UTC 2 December to ~150 m at 06 UTC 3 December (Fig. 4). The downward slope of the isentropes within the capping layer of strong static stability is partially due to increased warm air advection associated with the strengthening southerly flow and, as we show later, also due to tilting and displacement of the CAP.

Surface conditions at station SM6 on the valley floor at the extreme southern end of the SLV and immediately in the lee of the Traverse Mountains (Fig. 5) remained quiescent (speeds less than 3 m s^{-1}) and were similar to those observed throughout most of the SLV until 00 UTC 3 December at which time the first burst of warm (>10 ^{o}C), dry (dew point temperatures < -5 ^{o}C), and windy (speeds greater than 7.5 m s^{-1}) conditions penetrated for a brief time to the surface. CAP conditions resumed at this location until 03 UTC followed by a second intrusion of warm, dry, windy conditions through 0830 UTC (Fig. 5). Another short period of CAP conditions was followed by the third warm, windy burst from 10-13 UTC. The causes for these abrupt changes in surface conditions are explored throughout this paper.

The disturbance period in the valley concludes after ~15 UTC 3 December as the trough axis passes over the region bringing a sharp reduction in the winds aloft and surface conditions at the south end of the valley return roughly to those observed the day before (Fig. 5). Hence, the disturbance period is more complicated than the hypothesis provided by Wei et al. (2013) that it was due to the passage of a weak cold front.

3.1.3 Persistence

Following the trough's departure, the CAP returns to a quiescent state, providing continued cold temperatures and high levels of pollution as ridging builds over the intermountain west on 4-6 December (Fig. 2). During this phase, the CAP eventually developed a stratocumulus-capped boundary layer and periods of surface fog (red shading Fig. 2b) leading to travel delays and, unfortunately, contributing to the crash of a small aircraft to the north of the SLV near Ogden, UT on 6 December.

3.1.4 Breakup

The long-lived IOP-1 CAP was finally destroyed late on 6 December by cold-air advection aloft, internal convection, and enhanced winds associated with a much stronger shortwave trough moving into the region (Wei et al. 2013). The breakup of the valley stratification was accompanied by a reduction in the particulate pollution and a return to healthier air quality (Fig. 2).

3.1.5 Forecast Uncertainty

During this CAP event, forecasting the extent of the trough-CAP interaction on 3 December was particularly difficult. Operational and research numerical weather prediction guidance did not resolve the details associated with this weak trough passage and the limited impact it had on improving air quality in the valley. For example, while the retrospective research simulations completed by Wei et al. (2013) captured many of the general features associated with IOP-1, their simulation fared poorly during the Disturbance Phase with wind speed and direction errors as large as 10 m s^{-1} and 90° respectively, and temperature errors greater than 2.5° C below 700 hPa. To better understand the unresolved processes that contributed to the CAP evolution during the Disturbance phase, we now turn to detailed analyses of PCAPS observations.

3.2 Surface Temporal Evolution

The abrupt changes in surface meteorological conditions evident in Fig. 5 are caused by a sequence of displacements of the CAP along the valley axis. To better understand these displacements, hourly surface temperature gridded analyses at ~100 m horizontal resolution are created from all available surface temperature observations using a Barnes horizontal distance weighting (Barnes 1964) of the departures of the observed temperatures from the temperature estimated for that elevation from the hourly vertical profiles of temperature described in Section 2b (Figs. 6-9). The relatively dense network of temperature observations available in the SLV during this IOP reduces the sensitivity of the resulting analyses to the technique, e.g., very similar temperature analyses have been obtained for this period using a two-dimensional variational analysis technique (Tyndall and Horel 2012).

The overall dependence of temperature on elevation is immediately apparent from the surface temperature observations and analyses in Figs. 6-9. For example, the string of HOBO temperature sensors along Harker's Ridge (Fig. 1) at 0000 UTC (Fig. 6a) transitions from low temperatures (blue shades) in the valley to much higher temperatures on the western slopes of the valley (yellow and orange shades) before again dropping at the upper reaches of the Oquirrh Mountains (blue shades). Prior to 0000 UTC, the temperatures in the lowest elevations of the SLC were nearly uniform (not shown).

The first CAP displacement in the valley is evident at 0000 UTC, where the leading edge of the CAP is shifted northward, forming a roughly east-west frontal zone (Fig. 6a). Warm air

(5-10° C) and southerly winds penetrate to the surface to the south of the front, while cold air (~0° C) and northerly winds are present to the north. This initial CAP displacement is reversed over the next two hours (Fig. 6 b, c) as the CAP edge advances southward at the lowest elevations, eventually abutting the Traverse Mountains to the east of the Jordan Narrows. The southwest corner of the valley remains out of the CAP at that time with southerly flow continuing over the Traverse Mountains in that region.

A second northward CAP displacement is initiated at ~0300 UTC as strong winds and warm temperatures again surface along the southeastern portions of the valley (Fig. 5 and Fig. 6d). The southerly flow is particularly strong and warm along the lee slopes of the Traverse Mountains. The edge of the CAP then moves progressively northward through the valley, reaching its northernmost excursion at ~0600 UTC (Fig. 7 a,b,c). At that time high temperatures (~10° C) and strong southerly winds (7-10 m s^{-1}) are reported throughout the southern 2/3 of the valley, while light winds and temperatures around 0° C persist within the displaced CAP. The temperature gradient across the leading edge of the CAP is ~10° C over 2 km. The pronounced tendency for the displacement of the CAP to be enhanced over the western portion of the SLV arises in part from its higher elevation as well as the unimpeded flow towards the Great Salt Lake on that side of the Valley.

Despite continued strong southerly flow aloft, the leading edge of the CAP again reverses course between 0700 and 0800 UTC, returning southward through the valley (Fig 7d and 8a). As the cold air advances, winds to the north of the front become coherent in strength and direction, flowing from the NW to SE then turning south along the valley axis (Fig. 8a). Meanwhile, strong south winds continue to the south of the front indicating convergence along the leading edge of the cold air. As the CAP subsumes observing sites throughout the valley, the cold frontal temperature drop is nearly identical in magnitude to the previous warm frontal rise, which produces the step changes apparent in individual time series (e.g., Fig. 5). By 0900 UTC (Fig. 8b), the cold front encroaches on the Traverse Mountains in the southeastern sections of the SLV. As before, high temperatures and strong winds continue along the southwestern portion of the valley and near the crest of the Traverse Mountains.

The third and final CAP displacement commences between 1000 and 1200 UTC as the frontal boundary again moves northward re-establishing a position across the valley center (Fig. 8c,d and Fig. 9a). This third displacement is shorter lived, and as the winds aloft diminish after 1200 UTC (Fig. 4), the cold front mobilizes southward for the final time (Fig. 9b). By 1500 UTC (Fig. 9d), the CAP has returned throughout the valley and penetrates south through the Jordan Narrows into the neighboring Utah Valley. This reversal in the gap flow effectively marks the end of the disturbed CAP conditions and a return to the quiescent and horizontally homogenous CAP ensues.

3.3 Mountain Wave

The north-south displacements of the CAP evident in the hourly surface temperature analyses and other earlier figures result in part from the southerly flow crossing over the Traverse Mountains into the SLV. The vertical profiles of potential temperature and wind speed upstream of the Traverse Mountains are shown at 0600 UTC 3 December in Fig. 10a, which corresponds to the furthest northward displacement of the CAP. Disregarding the sharp surface-based radiational inversion, the profiles suggest upstream conditions can be characterized at that time as a two-layer stably-stratified fluid: nearly constant wind speed and potential temperature above 1750 m with 6K lower potential temperature below 1650 m with increasing wind speeds through the lower layer and extending into the intervening strong stable layer.

Ignoring the surface based inversion, it is possible to compute the internal Froude number from this profile as

$$Fr = \frac{U}{\sqrt{g'h}} \tag{2}$$

where U is the mean wind speed (~6 m s^{-1}), h is the height of the interface (~300 m),

$$g' = \frac{\Delta\theta}{\theta} g \tag{3}$$

is the reduced gravity where Δθ is the change in temperature across the capping layer (~6 K) and θ is the mean profile temperature (~297 K). With these approximations $Fr \approx 0.8$, indicating that the upstream mean flow is slightly slower than the fastest linear shallow water gravity waves. It is likely, then, that as the flow passes over the crest of the Traverse Mountains and thins (e.g., h reduced to ~100 m) it transitions to a super-critical state (Fr > 1). Following the hydraulic flow analogy, such a flow is expected to produce a mountain wave with strong downslope winds with non-linear effects including a downstream hydraulic jump (Durran 1986). Similar flows have previously been documented over the Traverse Mountains during diurnal CAPs by Chen et al (2004).

The impact of the mountain wave along the fall line of the Traverse Mountains is shown in Fig. 10c. Consider first the conditions at the time of the upstream sounding (0600 UTC). All stations from the ridge crest (SM1) to the valley floor in the lee (SM6) report the same potential temperature, ~ 297 K, which is consistent with air in the upstream stable layer at ~1700 m being lifted up and over the ridge while the lower upstream layers are blocked by the barrier. Wind speeds at the crest (SM1- black curve) and near the valley floor (SM5- red; SM6- dark blue respectively) are equally strong at this time and occasionally the winds at the base of the slope are stronger, reflecting acceleration of the flow. (Consistently weaker winds at intervening sites, such as SM4, light blue curve, reflect siting more than atmospheric conditions.)

The pulsing of mountain-waves throughout the Disturbance phase causes the along-slope potential temperature profile to abruptly switch between stratified and adiabatic states (Fig. 10c). For example, the ridge-to-valley potential temperature difference is ~12 K at 0250 UTC, whereas just 20 minutes later it is nearly zero (a reminder that Fig. 5 is the blue curve in Fig. 10 c, d). Periods of along-slope adiabatic flow are accompanied by the penetration of strong southerly winds to the valley floor, whereas weak northerly flow near the valley floor coincides with stratification. The restratification of the CAP once the southerly flow lessens is clearly evident after 1300 UTC with no change in the conditions at the top (SM1) and progressively lower potential temperatures down the lee slope into the valley.

To visualize in greater detail the impact of the flow across the Traverse Mountains, an idealized quasi-two dimensional Large-Eddy-Simulation is shown in Fig. 11. The simulation is initialized from temperature and wind profiles similar to those shown in Fig. 10a and uses a 50 km cross section of the SLV beginning south of the Traverse Mountains, extending north across the ISS sites, and terminating at the Salt Lake International Airport. The domain is 1 km wide to allow 3-D turbulence and uses open boundary conditions at the downwind (northern) boundary and a Rayleigh damping layer at the southern boundary that maintains a constant inflow profile. The near-surface inversion in the upstream sounding is extrapolated to match the observed surface temperature ISS-S within the SLV, which was 285 K. Radiation is neglected, as are sensible heat fluxes at the surface, and friction is parameterized using a Monin-Obukov surface layer scheme. The horizontal grid spacing is 50 m and there are 100 vertical levels stretched over 10 km. The vertical resolution is nominally 30-50 m within the valley. The simulation is run for 1-hr to capture the immediate response of the downstream CAP to the upstream stratified flow over the topography.

After 1 h, a pronounced mountain wave, hydraulic jump, and CAP displacement are apparent (Fig 11b). The low-level upstream flow is partially blocked such that the depth of the cold lower layer increases until it surmounts the ridge and spills down the lee-slopes. As we speculated above, the Froude number at the mountain crest exceeds the critical value within the overtopping flow. The flow aloft behaves similarly, represented by perturbations in the height of the 300 K isentrope. Accompanying the thermal perturbation of the wave is a marked increase in wind speed above the ridge crest and extending down the lee slope. The lee-side along-slope flow is ostensibly adiabatic with constant speed in excess of 10 m s^{-1}, consistent with observations in Fig. 10c,d.

The flow separates from the surface near the base of the lee slope in a pronounced hydraulic jump. The presence of the upstream inversion layer is well known to favor such hydraulic jumps, lee waves, and boundary layer separation (Vosper 2004; Jiang et al. 2007). The surface flow within the jump region is reversed and the air becomes turbulently mixed, reducing the stratification and eroding the surface based inversion. Consequently a front forms separating the comparatively quiescent near-surface CAP conditions to the north from the better-mixed and windier conditions to the south.

The front shown in the numerical simulations suggests a link between the strength of the mountain wave and the timing of the CAP advance and retreat throughout the valley. For example, the northward displacement of the CAP between 0300 and 0600 UTC correspond to a time of increased downslope flow, whereas the frontal reversal is linked with a modest decrease in the strength of the downslope winds.

3.4 Advance and Retreat of the CAP

While the mountain waves caused the CAP to retreat and advance in the extreme southeastern end of the SLV three times on 3 December, a single disruption of the CAP was centered near 0600 UTC 3 December at the ISS sites (Fig. 2). Figure 12 shows in more detail this ~3 h period when the CAP retreated northward past the ISS sites temporarily providing clean air (low aerosol backscatter). The retreat of the CAP is synonymous with the passage of a warm front, which is marked by a gradual reduction in the height of the aerosol layer followed by rapid reduction in aerosol concentration, a 7 K temperature rise, and a burst of strong southerly winds (Fig. 12). As the front continues northward past ISS-S, there is a ~12 minute lag before its passage at ISS-N, which is one kilometer away, giving a propagation speed in the along valley direction of ~1.5 m s^{-1}. Using these values, the width of the frontal zone is ~1 km and the front-normal temperature gradient is ~7 K km^{-1}. The winds on the warm side of the front are around 8 m s^{-1} from the south while those within the CAP are nearly zero.

Figure 13 shows a radiosonde launched at ISS-S just 5 minutes before the warm front passes. The sounding ascends through a sharp surface inversion and a strongly stable capping layer. The depth of the stable layer has clearly diminished leading up to this launch (cf. Fig. 2). As the front passes and the surface potential temperature increases by 7 K, the thin surface-based inversion layer is removed and replaced by a shallow well-mixed layer beneath the still present capping layer. Based on the model simulation shown in Fig. 11 and dynamical reasoning associated with mountain lee waves, it is likely that the sharply higher potential temperature and cleaner air behind the warm front is associated with the air flowing from aloft upstream of the Traverse Mountains descending into the SLV and mixing with the much colder air within the CAP.

In contrast to the gradual thinning and quiescent prefrontal conditions associated with the warm front, the cold front arrives with strong northerly winds (4-5 m s^{-1}) and an abrupt 200 m increase in the depth of the aerosol layer (Fig. 12). This frontal "head" is shown in more detail in Fig. 14 and moves much more quickly than the warm front, advancing between the ISS sites in just 5 minutes, giving a propagation speed of ~3.5 m s^{-1}, which is more than twice that of the warm front. The northerly flow within the cold air behind the front combined with the opposing southerly flow of ~5-7 m s^{-1} implies strong convergence.

In the wake of the frontal head, the aerosol layer depth decreases and high amplitude waves develop (Fig 14). This morphology is consistent with the characteristics of an advancing gravity current, e.g. an elevated head, convergent opposing flow, and mixing via Kelvin-Helmholtz waves behind the front (Simpson 1997). Moreover, the ceilometer data suggest that the upstream two layered air mass (Fig 14) is lifted over the gravity current head (high aerosol backscatter), with evidence of the frontal disturbance as much as 300 m AGL. This evolution closely resembles laboratory and numerical simulations of gravity currents propagating into a two layer stratified environment (Simpson 1997; White and Helfrich 2012).

The differences between the retreat and advance of the CAP likely relates to differences in the front-relative shear profiles, which profoundly influence gravity current dynamics (Markowski and Richardson 2010). During the warm frontal passage, the CAP advances in the same direction as the upstream wind and opposite to the shear vector. Such sheared profiles generally produce low amplitude gravity current heads. In contrast, the cold front has strong flow within the lowest layers of the cold-air and propagates against the ambient flow such that the front-relative shear vector is reduced, which leads to a taller frontal head, stronger updraft, and more vigorous mixing behind the front (Simpson 1997; Markowski and Richardson 2010). Previous investigations of gravity currents have found that the mixing behind the frontal nose can strongly impact heat and momentum fluxes within the stable boundary layer (Sun et al. 2002).

3.5 CAP Tilt

The model simulation in Fig. 11 suggests that the displaced CAP may be inclined to the north such that the depth of the cold air increases over the span of the SLV, particularly considering that the valley is sloping downwards as well. Fig. 15 contrasts the vertical profiles of potential temperature and wind over a distance of 19.2 km between ISS-S and KSLC near the end of the Displacement Phase. The depth of the CAP at KSLC is clearly 200 m deeper than at ISS-S when the leading edge of the CAP is located ~3 km to the south of ISS-S.

CAPs are known to develop such sloping surfaces in response to both static and dynamic forcing. The static response is the CAP adjustment to the regional pressure gradient (Petkovšek and Vrhovec 1994, Zängl 2003) while the dynamic response relates to the wind stress across the top of the CAP (Petkovšek and Vrhovec 1994, Gubser and Richner 2001). Following Zängl (2003), the magnitude and shape of the static displacement can be approximated by

$$\Delta z = T\sqrt{\frac{dP}{dx}\frac{2R}{Pg\Delta\gamma}}\sqrt{\Delta x} \tag{4}$$

where T, P, and $\frac{dP}{dx}$ are representative values for the temperature, pressure, and pressure gradient immediately above the CAP and $\Delta\gamma$ is the difference between the CAP and ambient lapse rates. The expression indicates that the depth of the cold-air is proportional to the square root of the distance from the leading edge of the cold air and that the smaller the lapse rate differences, the greater inclination of the CAP required to balance the regional pressure gradient (Zängl 2003).

Using values derived from the soundings shown in Fig. 15 and an estimate of the large-scale pressure gradient from ERA-interim reanalyses at 12 UTC (~1.25 x 10^{-3} Pa m^{-1}) we superimpose onto Fig. 15 (blue triangle) the estimated depth of the CAP at KSLC from (4). This approximation underestimates the depth of the cold-air by ~150 m at KSLC. It is likely then that dynamical wind stresses impact the CAP structure as well.

To account for the dynamic component of the displacement, we consider an antitriptic balance (Sun et al. 2013) between the perturbation pressure gradient within the CAP and the momentum flux convergence due to Reynolds shear stress across the cold-pool top

$$\frac{1}{\rho}\frac{\partial P'}{\partial x} = \frac{\partial u'w'}{\partial z} \tag{5}$$

Following Li et al. (2009), the pressure perturbation at the surface can be determined from the vertically integrated temperature anomalies

$$\begin{aligned} P'(z=0) &\approx \frac{\rho g}{T}\int_{z=0}^{z=\Delta z} T'(z)\,dz \\ &\approx \frac{\rho g\gamma}{T}\frac{\Delta z^2}{2} \end{aligned} \tag{6}$$

Where ρ and T are reference values for density and temperature, Δz is the vertical CAP displacement away from horizontal, and γ is the lapse rate, which is assumed to be constant. Integrating (6) once within the CAP and once within the warm air, the internal pressure gradient is then approximated as

$$\frac{1}{\rho}\frac{\Delta P'}{\Delta x} \approx \frac{g\Delta\gamma}{2T}\frac{\Delta z^2}{\Delta x} \tag{7}$$

Where $\Delta\gamma$ is again the difference in lapse rates. Next, we approximate the momentum flux divergence as

$$\frac{\partial u'w'}{\partial z} \approx \frac{u'w'_{top} - u'w'_{bot}}{H} \approx \frac{k_m \frac{\partial u}{\partial z}}{H} \approx k_m \frac{\Delta u}{H^2} \tag{8}$$

where we assume that the momentum flux at the top of the layer is much greater than at the surface, H is the depth of the shear layer, and ΔU is the wind speed difference across H. The eddy diffusivity for momentum, k_m, is itself a function of the flow, and can be approximated for the "upside boundary layer" based on the Richardson number (Kim and Mahrt 1992).

Combining (7) and (8) and then solving for the dynamic displacement yields

$$\Delta z_{dyn} = \sqrt{\frac{2T}{g}\frac{k_m \Delta u}{H^2 \Delta\gamma}\,\overline{\Delta x}}. \tag{9}$$

Again using values from the soundings in Fig. 15 (H= 400 m, T = 280 K, $\Delta u = 17$ m s^{-1}, k_m= 3 m^2 s^{-1}, $\Delta\gamma = 2.98 \times 10^{-2}$ K m^{-1}) we compute Δz_{dyn} and add the result to the static displacement. The resulting approximation for the idealized CAP top matches more closely the elevation difference of the CAP at ISS-S and KSLC (cyan triangle, Fig. 15).

We conclude, then, that the observed CAP geometry reflects a three-way balance between the perturbation pressure gradient, the pressure gradient aloft, and the wind stress. This balance can, however, be easily disrupted by changes in the wind speed. For example a sudden decrease in the wind shear would cause the internal pressure gradient to be out of balance, and prompt a southward rush of cold-air until a new balance is established. This may help explain the advance and retreat of the CAP that was described in the above sections as well as the gravity current characteristics of the advancing cold air.

3.6 Kelvin-Helmholtz Instability

Many high frequency (order minutes) waves are observed during IOP-1 (cf. Fig. 11). Amongst these waves we are particularly interested in those resulting from Kelvin-Helmholtz instability, which is a dynamic instability occurring in stratified shear flows when the kinetic energy available from shear exceeds the work required to move a parcel against the stratification. When this condition is met, Kelvin-Helmholtz waves (KHW) develop, evolving from small perturbations into breaking waves that mix properties across the stratification (Nappo 2002). Formally this condition is given by the gradient Richardson number,

$$Ri = \frac{N^2}{\left(\frac{\partial u}{\partial z}\right)^2 + \left(\frac{\partial v}{\partial z}\right)^2} \tag{10}$$

where N is the Brunt–Väisälä frequency, and the terms in the denominator are the components of the vertical shear. KHW are an important mixing mechanism in stratified geophysical flows (Fernando 1991) and have been regularly documented in the stable boundary layer and CAPs, often associated with low-level jets (Newsom and Banta 2003; Pinto et al. 2006; Flamant et al. 2006).

During IOP-1, KHW are first observed during the onset of the accelerating winds aloft. For example, Fig. 16a shows a sequence of high frequency (~1 cycle per minute) waves that culminate in a pronounced KHW billow that inverts the aerosol gradient within the wave crest. The folding of low aerosol air beneath high aerosol air suggests that these waves mix pollution from near the surface into the layers aloft, and presumably act similarly on the temperature profile.

A contemporaneous sounding at KSLC shows that the KHW are centered within a weakly stable layer between the surface-based inversion and the capping layer aloft. The wind shear across this layer is modest, but the Richardson number is nonetheless near the critical value for KHI ($Ri < 0.25$) due to the reduced static stability in that layer

At ~0400 UTC 3 December, winds aloft increase to ~10 m s^{-1} and KHW become a dominant feature in the aerosol backscatter profiles at ISS-S. Figure 16b shows a sequence of these KHW wherein 100 m amplitude waves occur once every 3 minutes. The first three waves successively grow in amplitude, and the 4th and 5th waves appear to have broken down into turbulence or smaller scale waves. The Richardson number, here evaluated from our time-height data, is near critical over a deep layer. However, since the time-height temperature and wind data lack the vertical and temporal resolution to resolve fine scale structures in the CAP, it is likely that the minimum values for Ri are lower than those calculated here.

Later, at ~1100 UTC 3 December (Fig. 16c), the winds aloft reach their peak strength of ~15 m s^{-1} and strong shear extends over the depth of the CAP. In fact, the shear is now enhanced by a counter current of northerly flow near the surface associated with the southward motion of the CAP. Correspondingly, Ri is reduced to near its critical value over most of the CAP depth. The KHW now have amplitudes upwards of 200 m, and appear to loft aerosols deep into the clear air above. The dominant period of these waves remains ~3 minutes.

As evident in earlier results as well, it is interesting to note that the CAP is not destroyed despite the strong wind shear, near critical Ri, and active KHW. Competing processes must offset the turbulent heat fluxes arising from the KHW, which would tend to remove the CAP stratification over time. We suspect that the vertical differential temperature advection across the CAP is responsible for maintaining its strength. For example, the northerly flow at the surface is continually feeding cold-air from deeper portions of the CAP into the region surrounding ISS, where these waves are active.

3.7 Basin-Scale Internal Waves

A noticeable feature of the Disturbance Phase of IOP-1 is the presence of SLV-scale internal waves. Relatively low frequency, long (basin-scale) wavelength phenomena such as baroclinic seiches are known to occur within stratified lakes (Csanady 1972; Monismith 1985), but have not been thoroughly documented in atmospheric CAPs (Largeron et al. 2013).

Such basin-scale internal waves (BSIW) appear to be manifest during IOP-1 as oscillations in the depth of the CAP superimposed upon the broader trends associated with the passage of the short-wave trough (Fig. 17). Visual inspection of the potential temperature and aerosol backscatter profiles suggests that the waves have a period of ~3 hrs., and arrive with a steep increase in depth but then depart with a more gradual thinning. We attempt to isolate the properties of these BSIW by applying a 1-5 hr band-pass filter to independent time series of surface pressure at ISS-S (1-min resolution) as well as the 1500-1800 m layer-averaged meridional wind and potential temperature at ISS (Fig. 17b). This filter removes lower frequency variations associated with synoptic-scale and diurnal fluctuations, high frequency variations due to micro-scale processes (e.g. KHW), and preserves the frequencies associated with the waves of interest.

The filtered data show that increases in the depth of the aerosol layer tend to correspond to increases in the surface pressure and decreases in layer mean temperature (Fig. 17b, i.e., a deeper CAP with higher aerosol concentration is accompanied by higher pressure and lower temperature). The meridional component of the wind generally reverses during the wave cycle, oscillating between more northerly and southerly along valley flow. This wind reversal is important in redistributing pollution within the CAP.

These oscillations are coherent over the scale of the SLV, appearing with comparable amplitude (~1 hPa) at each of the 7 ISFS sites (Fig. 17c). There is an ~1hr time lag between ISFS1 and ISFS7, which are at the north and south ends of the valley, respectively, and separated by about 31.4 km (see Fig. 2). Spectral analysis of these time-series confirms that the dominant BSIW period is between 3 and 4 hrs (not shown).

To further demonstrate the link between surface pressure and CAP structure, we examine one of these waves as it passes over the Harker's ridge transect between 0515 and 0845 UTC 2 December (Fig. 18a). From these profiles it is apparent that the oscillation takes the form of rises and falls in the depth of the surface-based layer of cold air relative to a mean state. The maximum amplitude in temperature variations occur within the layer between 1500 and 1800 m, which coincides with the transition layer that separates the surface-based nocturnal inversion from the capping layer aloft. This residual layer is apparent in the individual profiles as a nearly adiabatic lapse rate generally centered at about 1600 m.

We associate surface pressure perturbations with the temperature perturbations by integrating Eq. 6 over the height of the transect in Fig. 18a. Figure 18b shows the computed perturbations as the wave passes and confirms that as the CAP rises (falls) the surface pressure increases (decreases) by ~0.4 hPa, giving a total amplitude of ~0.8 hPa which is consistent with the pressure perturbations measured throughout the valley (Fig 17c). The computed perturbations also capture the steep initial rise followed by the more gradual thinning seen in the aerosol backscatter (Fig. 17a).

The exact causal mechanism and nature of these BSIW is as of yet unknown. They may arise due to any of a number of forcings acting upon the stably stratified CAP. For example, it is possible that they are a response to an external forcing, such as the increasing winds aloft, or an internal forcing, such as katabatic flows or lake breezes that are known to occur within the SLV during CAPs. Regardless of their source, these BSIW are an important factor in local changes in the CAP. For example it is possible that these waves alter the CAP internal force balance and contribute to the advance and retreat of the cold air. Interestingly such phenomena do not appear to be previously documented in CAP literature.

4 Summary and Conclusions

In this paper we have documented the complex evolution of a CAP that was disturbed by a passing short-wave trough. We show that the initially horizontally homogenous stratified air mass was disrupted by a series of along valley displacements, frontal passages, internal waves, and turbulent mixing. To synthesize these elements of the trough-CAP interaction we present here a schematic of the CAP evolution (Fig. 19) using insights from the observational data and the numerical simulation.

The stages of the CAP disruption are as follows:

(a) At the onset, a quiescent and horizontally homogenous two-layered CAP resides in the valley. Synoptic scale warming aloft modulates the upper stable layer, while the surface based inversion is affected by diurnally varying sensible heat fluxes. The layers are partially separated by a residual layer of weaker stability (Fig. 19a).

(b) Winds above the CAP increase as a disturbance approaches. A mountain wave develops in the stratified cross barrier flow over the upstream topography, generating downslope warming and accelerated winds. The plunging flow displaces and erodes the surface inversion, forming a frontal interface. Increased shear leads to KHW, especially at the top of the surface inversion layer (Fig. 19b).

(c) The CAP tilts upward in the down wind direction, establishing a force balance between the internal hydrostatic pressure gradient, the external pressure gradient, and the wind stress acting on the CAP. As the CAP tilts, its southern edge advances through the valley as a warm front, providing warmer, windier, and cleaner air to southern locales (Fig. 19c, note that in this panel the schematic includes observed potential temperatures from soundings and surface stations at ~1100 UTC 3 December).

(d) Some perturbation, such as a temporary reduction in wind stress or a wave modulated change in depth, disrupts the CAP force balance. The CAP tilt partially collapses due to the unbalanced internal pressure gradient, sending a shallow density current propagating upwind through the valley and restoring the surface based inversion. Enhanced KHW mixing occurs in the wake of the density current (Fig. 19d).

Stages b-d repeat as the force balance is restored leading to a sequence of frontal advances and retreats over upwind portions of the valley. Meanwhile northern locales remain within the CAP throughout the evolution. Finally, the winds aloft diminish and the CAP tilt collapses for a final time, restoring horizontally homogenous and quiescent CAP conditions throughout the valley.

While this simple schematic summary relies primarily on data from IOP-1, it nonetheless fits well with observations from many other CAPs, which are common in the SLV. For example, a similar sequence of step-like frontal temperature changes was observed at ISS-S during PCAPS IOP-4 (not shown). Moreover, many of the details of the IOP-1 CAP are similar to the evolution of the CAPs described by Whiteman et al. (2001) and Flamant et al. (2006). Namely, a CAP is displaced in strong pre-frontal downslope winds leading to a warm front that provides partial or complete valley ventilation. In the present case, the CAP displacement is reversible, and CAP conditions are restored after winds abate. In other instances, however, a CAP may be completely removed, suggesting that irreversible turbulent mixing and spillover at the downwind end of the basin play an important role in CAP destruction.

We conclude by noting that many of the key features in the trough-CAP interaction are meso- and micro-scale processes that are typically either poorly resolved or altogether unresolved in numerical forecast guidance. These unresolved processes strongly impact the CAP, and thus the forecasts for air quality. To further address the sensitivity of CAP removal to mountain waves, hydraulic jumps, KHW, and BSIW a companion study using a larger set of idealized large-eddy simulations than the single simulation used to generate Fig. 11 will be forthcoming.

Acknowledgements

We greatly appreciate the individuals and entities involved in PCAPS: staff from agencies (NCAR Earth Observing Laboratory ISS and ISFS Groups, Utah Division of Air Quality, Utah Department of Transportation, National Weather Service Forecast Office, Dugway Proving Ground, and Kennecott Utah Copper); faculty, staff and students at academic institutions (University of Utah, San Jose State University and San Francisco State University), and other volunteers. Of particular note are the individuals in the Mountain Meteorology Group at the University of Utah: C. David Whiteman for his leadership of the project and feedback on this research; Sebastian Hoch for his installation of the HOBO sensors and other data collection efforts; Joseph Young for his processing of the ceilometer data; and Erik Crosman for his feedback on this research. The support and resources from the Center for High Performance Computing at the University of Utah is gratefully acknowledged. This research is supported by Grant ATM-0938397 from the National Science Foundation.

References

Barnes SL (1964) A technique for maximizing details in numerical weather map analysis. J Appl Meteorol 3:396–409

Beard JD, Beck C, Graham R, Packham S, Traphagan M, Giles R, Morgan JG (2012) Winter temperature inversions and emergency department visits for Asthma in Salt Lake County, Utah, 2003-2008. Env Health Pers 120:1385-1390

Bell RC, Thompson R (1980) Valley ventilation by cross winds. J Fluid Mech 96: 757-767

Chen Y, Ludwig FL, Street RL (2004) Stably stratified flows near a notched Transverse Ridge across the Salt Lake Valley. J Appl Meteorol 43: 1308-1328

Chow, F.K., De Wekker, S.F.J., and B. Snyder (eds). 2013. Mountain Weather Research and Forecasting: Recent Progress and Current Challenges, Springer, Berlin. DOI: 10.1007/978-94-007-4098-3

Csanady GT (1972) Response of large stratified lakes to wind. J Phys Oceanogr 2: 3–13.

Durran, DR (1986) Another look at downslope windstorms. Part I: The development of analogs to supercritical flow in an infinitely deep, continuously stratified fluid. J Atmos Sci 43:2527–254

Flamant C, Drobinski P, Furger M, Chimani B, Tschannett S, Steinacker R, Protat A, Richner H, Gubser S, Haberli C (2006) Föhn/CAP interactions in the Rhine valley during MAP IOP 15. Quart J Roy Meteorol Soc 132:3035-3058

Fernando HJS (1991) Turbulent mixing in stratified fluids. Annu Rev Fluid Mech 23: 455-493.

Gillies RR, Wang SY, Booth MR (2010) Atmospheric scale interaction on wintertime Intermountain West low-level inversions. Weather Forecast 25:1196-1210

Gubser and Richner 2001 'Investigations into mechanisms leading to the removal of the cold-pool in foehn situations'. Extended abstracts from MAP meeting at Schliersee. MAP Newsletter 15. Available at: http://www.map.meteoswiss.ch/map-doc/NL15/gubser2.pdf

Horel J, Splitt M, Dunn L, Pechmann J, White B, Ciliberti C Lazarus S, Slemmer J, Zaff D (2002) Mesowest: cooperative mesonets in the western United States. Bull Am Meteorol Soc 83:211-225

Jiang Q, Doyle JD, Wang S, Smith RB (2007) On boundary layer separation in the lee of mesoscale topography. J Atmos Sci 64:401–420

Kim J, Mahrt L (1992) Simple formulation of turbulent mixing in the stable free atmosphere and nocturnal boundary layer. Tellus 44:381–394

Largeron Y, Staquet C, Chemel C (2013) Characterization of oscillatory motions in the stable atmosphere of a deep valley. Boundary-Layer Meteorol 148:439-454

Lareau NP, Crosman E, Whiteman CD, Horel JD, Hoch SW, Brown WOJ, Horst TW (2013) The persistent cold-air pool study. Bull Am Meteorol Soc 94:51–63

Lee TJ, Pielke RA (1989) Influence of cold pools downstream of mountain barriers on downslope winds and flushing. Mon Weather Rev 117:2041-2058

Lee JT, Lawson RE, Marsh GL, Jr (1987) Flow visualization experiments on stably stratified flow over ridges and valleys. Meteorol Atmos Phys 37:183-194

Li Y, Smith RB, Grubišić V (2009) Using surface pressure variations to categorize diurnal valley circulations: experiments in Owens Valley. Mon Weather Rev 137:1753–1769

Malek E, Davis T, Martin RS, Silva PJ (2006) Meteorological and environmental aspects of one of the worst national air pollution episodes in Logan, Cache Valley, Utah, USA. Atmos Res 79:108-122

Markowski P, Richardson Y (2010) Mesoscale Meteorology in Midlatitudes. John Wiley & Sons, Ltd. 430, pp.

Marht L, Vickers D (2002) Contrasting vertical structures of nocturnal boundary layers. Boundary-Layer Meteorol 105:351-363

Monismith SG (1985) Wind forced motions in stratified lakes and their effects on mixed-layer shear. Limnol and Oceanogr 30:771-783
Nappo CJ (2002) An Introduction to Atmospheric Gravity Waves. Academic Press. 279 pp.
Newsom RK, Banta RM (2003) Shear-flow instability in the stable nocturnal boundary layer as observed by Doppler Lidar during CASES-99. J Atmos Sci 60:16–33.
Pataki DE, Tyler BJ, Peterson RE, Nair AP, Steenburgh WJ, Pardyjak ER (2005) Can carbon dioxide be used as a tracer of urban atmospheric transport? J Geophys Res 110:D15102.
Pataki DE, Bowling DR, Ehleringer JR, Zobitz JM (2006) High resolution atmospheric monitoring of urban carbon dioxide sources. Geophys Res Let 33:L03813
Petkovšek Z (1992) Turbulent dissipation of cold air lake in a basin. Meteorol Atmos Phys 47:237-245
Petkovšek Z, Vrhovec T (1994) Note on the influences of inclined fog lakes on the air pollution in them and on the irradiance above them. Meteorol Z 3:227-23
Pinto JO, Parsons DB, Brown WOJ, Cohn S, Chamberlain N, Morley B (2006) Coevolution of down-valley flow and the nocturnal boundary layer in complex terrain. J Appl Meteorol 45:1429-1449
Pope, III CA, Ezzati M, Dockery DW (2009) Fine-particulate air pollution and life expectancy in the United States. N Engl J Med 360:376-386
Rakovec J, Merše J, Jernej S, Paradiž B (2002) Turbulent dissipation of the cold- air pool in a basin: comparison of observed and simulated development. Meteorol Atmos Phys 79:195-213
Reddy PJ, Barbarick DE, Osterburg RD (1995) Development of a statistical model for forecasting episodes of visibility degradation in the Denver metropolitan area. J Appl Meteorol 34:616-625
Reeves HD, Stensrud DJ (2009) Synoptic-scale flow and valley cold pool evolution in the western United States. Weather Forecast 24:1625-1643
Reeves HD, Elmore KL, Manikin GS, Stensrud DJ (2011) Assessment of forecasts during persistent valley cold pools in the Bonneville basin by the North American Mesoscale model. Weather Forecast 26: 447-46
Schönlieb C-B (2012) Applying modern PDE techniques to digital image restoration. Mathworks Newsletter. Available at: http://www.mathworks.com/company/newsletters/articles/applying-modern-pde-techniques-to-digital-image-restoration.html
Silcox GD, Kelly KE, Crosman ET, Whiteman CD, Allen B (2012) Wintertime PM2.5 concentrations in Utah's Salt Lake Valley during persistent, multi-day cold-air pools. Atmos Environ 46:17-24
Simpson, JE (1997) Gravity currents in the environment and the laboratory. Cambridge University Press. 244 pp.
Skamarock WC, Klemp JB, Dudhia J, Gill DO, Barker DM, Duda MG, Huang X, Want W, Power JG (2008) A description of the advanced research WRF version 3. NCAR Tech. Note, NCAR/TN-475+STR, 113 pp.
Strang EJ, Fernando HJS (2001a) Entrainment and mixing in stratified shear flows. J Fluid Mech 428:349-386
Strang EJ, Fernando HJS (2001b) Vertical mixing and transports through a stratified shear layer. J Phys Oceanogr 31:2026-2048
Sun J, Burns SP, Lenschow DH, Banta R, Newsom R, Coulter R, Frasier S, Ince T, Nappo C, Cuxart J, Blumen W, Lee X, Hu X-Z (2002) Intermittent turbulence associated with a density current passage in the stable boundary layer, Boundary-Layer Meteorol 105:199–219
Sun J, Lenschow DH, Marht L, Nappo C (2013) The relationships among wind, horizontal pressure gradient, and turbulent momentum transport during CASES-99. J Atmos Sci (in press)
Tampieri F, Hunt JCR (1985) Two-dimensional stratified fluid flow over valleys: Linear theory and laboratory investigation. Bound.-Layer Meteor., 32, 257-279.
Tyndall DP, Horel JD (2013) Impacts of mesonet Observations on Meteorological Surface Analyses. Weather Forecast 28:254–269
U.S. EPA, cited 2013: National Ambient Air Quality Standards (NAAQS). [available online at http://www.epa.gov/air/criteria.html.]
Vosper SB (2004) Inversion effects on mountain lee waves. Quart J Roy Meteorol Soc 130:1723–1748
Vrhovec T, Hrabar A (1996) Numerical simulations of dissipation of dry temperature inversions in basins. Geofizika 13; 81-96
Wei L, Pu Z, Wang S (2013) Numerical simulation of the life cycle of a persistent wintertime inversion over Salt Lake City. Boundary-Layer Meteorol 148; 399-418
White BL, Helfrich KR (2012) A general description of a gravity current front propagating in a two-layer stratified fluid. J. Fluid. Mech., 711, 545-575.
Whiteman CD, Bian X, Zhong S (1999) Wintertime evolution of the temperature inversion in the Colorado Plateau Basin. J Appl Meteorol 38; 1103-1117.
Whiteman CD, Zhong S, Shaw WJ, Hubbe JM, Bian X, Mittelstadt J (2001) Cold pools in the Columbia basin. Weather Forecast 16; 432-447.
Wolyn PG, McKee TB (1989) Deep stable layers in the intermountain Western United States. Mon Weather Rev

117; 461-472.
Young J (2013) Investigation of wintertime cold-air pools and aerosol layers in the Salt Lake Valley using a laser ceilometer. MS Thesis. University of Utah. 118 pp.
Zängl G (2003) The impact of upstream blocking, drainage flow and the geostrophic pressure gradient on the persistence of cold-air pools. Quart J Roy Meteorol Soc, 129, 117–137.
Zängl G (2005) Winterime cold-air pools in the Bavarian Danube Valley Basin: Data analysis and idealized numerical simulations. J Appl Meteorol 44:1950-1971
Zhong S, Whiteman CD, Bian X, Shaw WJ, Hubbe JM (2001) Meteorological processes affecting evolution of a wintertime cold air pool in a large basin. Mon Weather Rev 129:2600-2613
Zhong S, Bian X, Whiteman CD (2003) Time scale for cold-air pool breakup by turbulent erosion. Meteorol Z 12:229-23

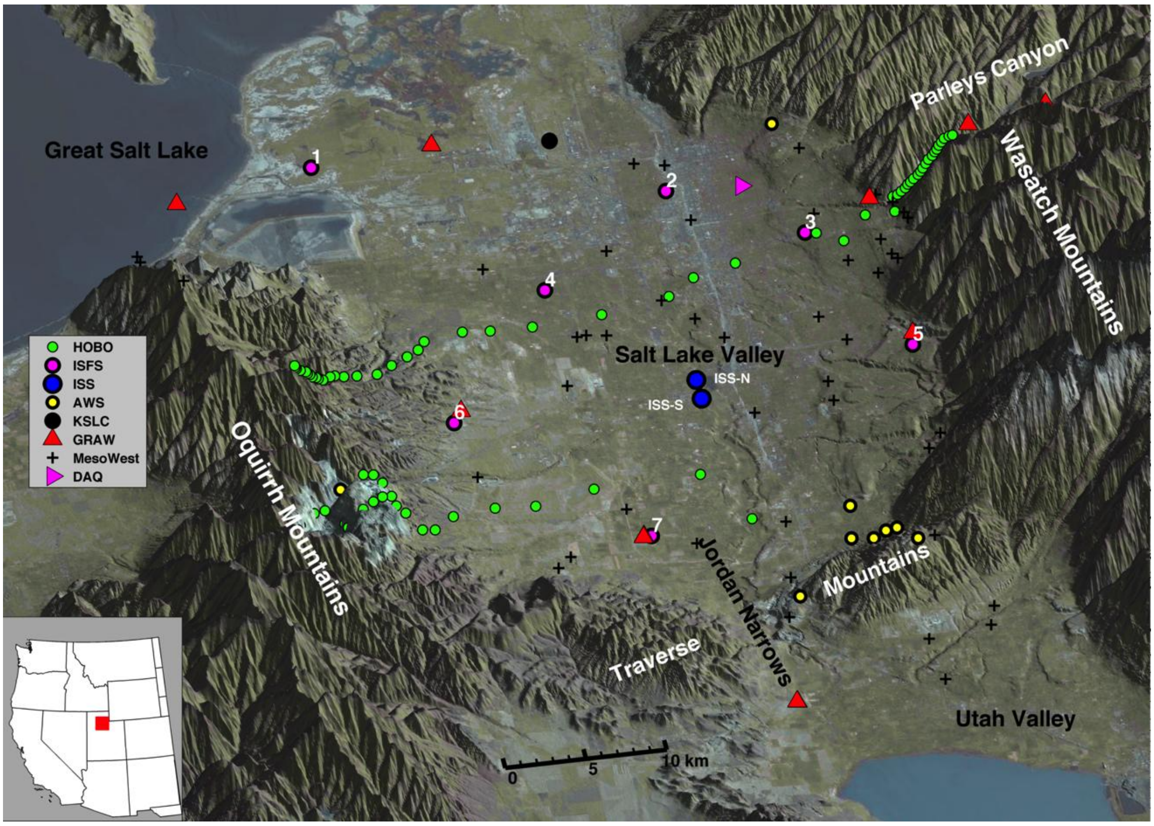

Fig. 1 Perspective view of the Salt Lake Valley showing PCAPS instrument locations and major topographic features (for further details see text and Lareau et al. 2013

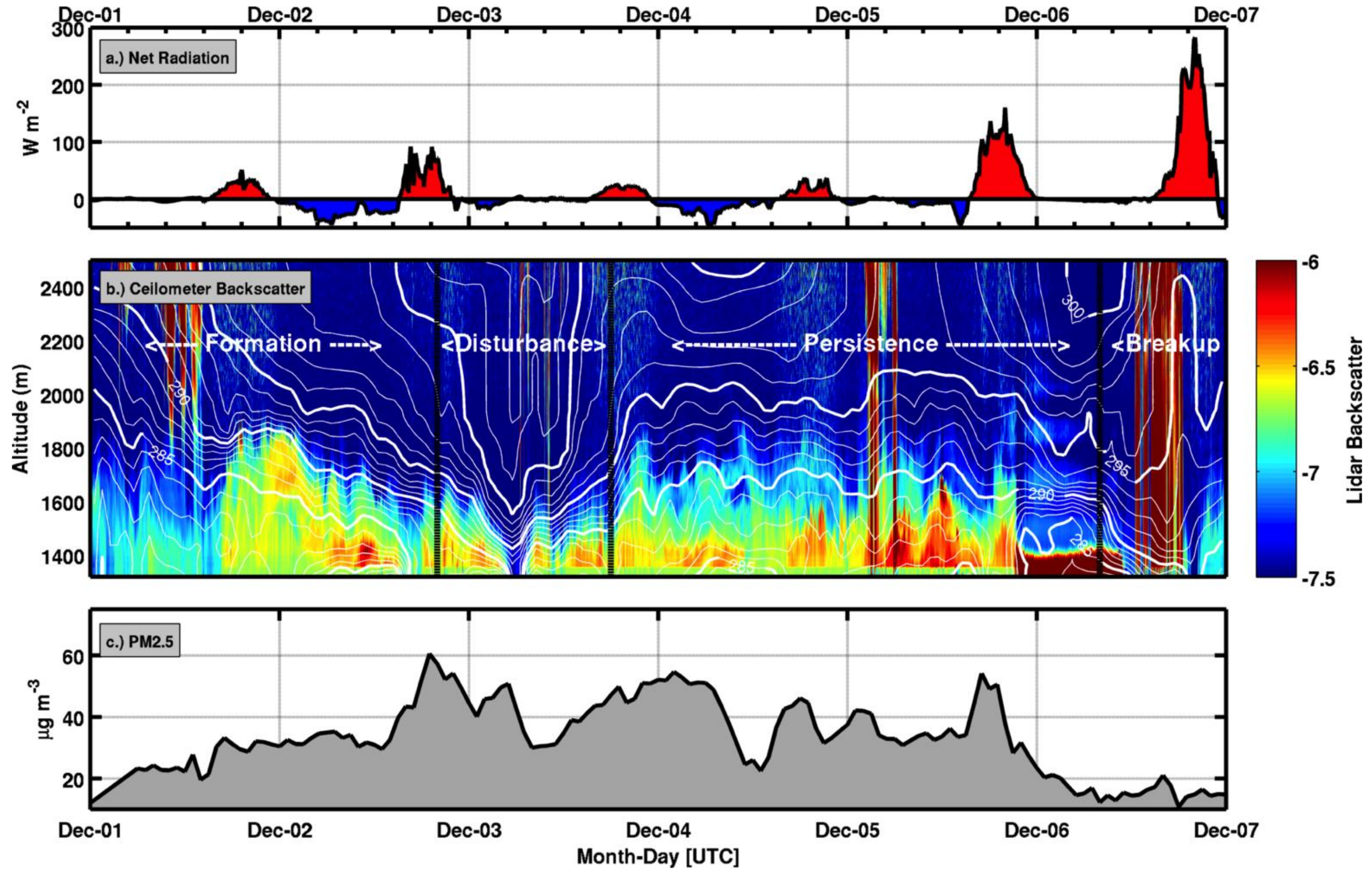

Fig. 2. Overview of PCAPS IOP-1. (a) Net radiation averaged over the seven ISFS stations in the SLV, (b) Time-height profile at ISS of potential temperature (contours at 1 K interval) and aerosol backscatter (shading) where yellow-orange (blue) shades reflect high (low) aerosol concentrations and dark red shades denote hydrometeors, (c) PM 2.5 concentration (μg m^{-3}) at DAQ site.

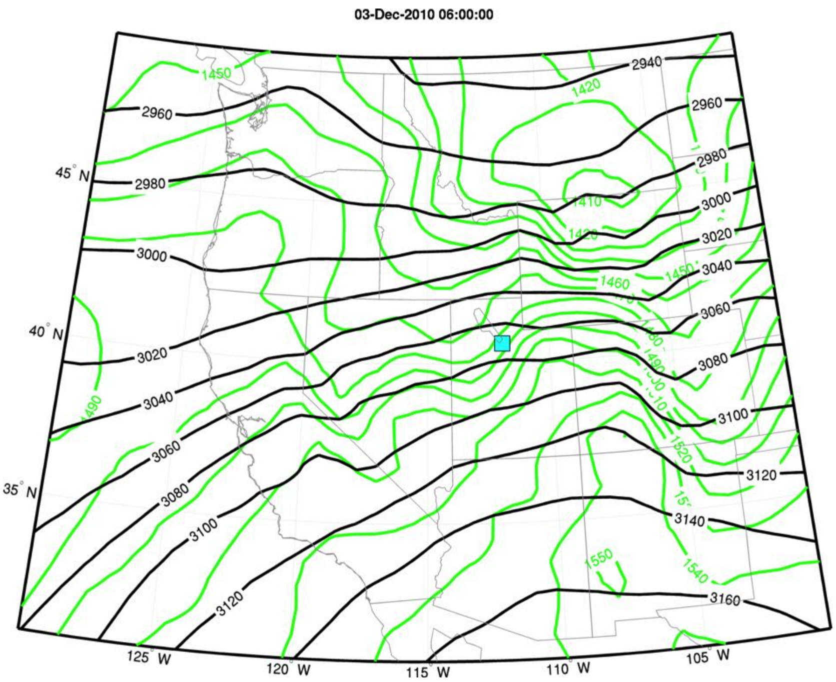

Fig. 3. European Centre for Medium-Range Weather Forecasts ERA-Interim reanalysis of the weak trough approaching Utah at 0600 UTC 3 December 2010. 700 hPa height (black contours at 20-m intervals) and 800 hPa height (green contours at 10-m intervals).

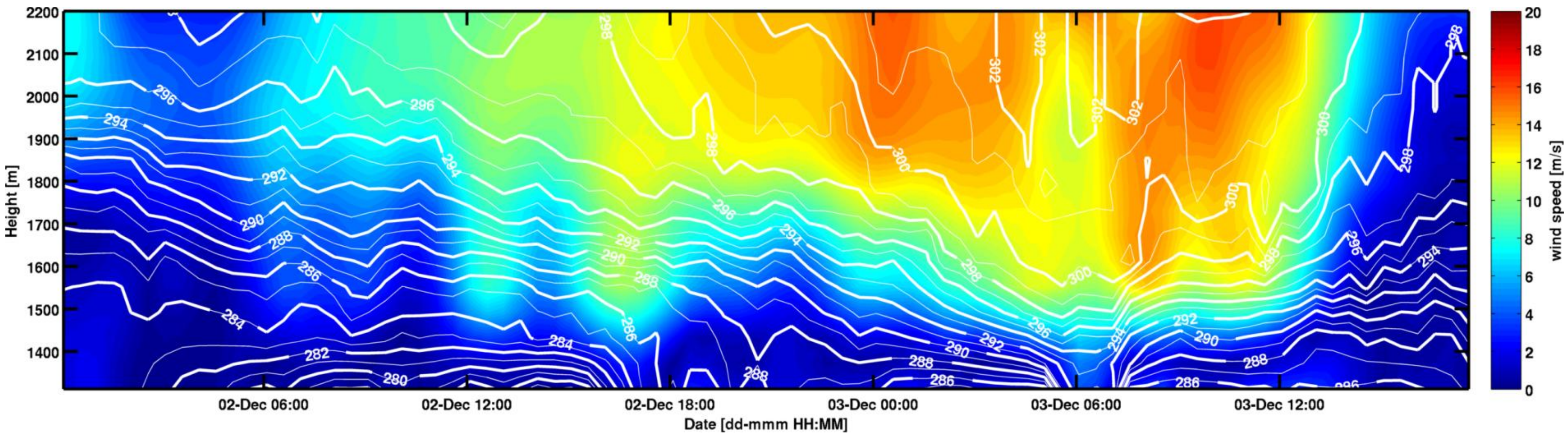

Fig. 4. Time height profile at ISS from 0000 UTC 2 – 1800 UTC 3 December of potential temperature (contours with heavy white lines every 2 K) and wind speed (shaded).

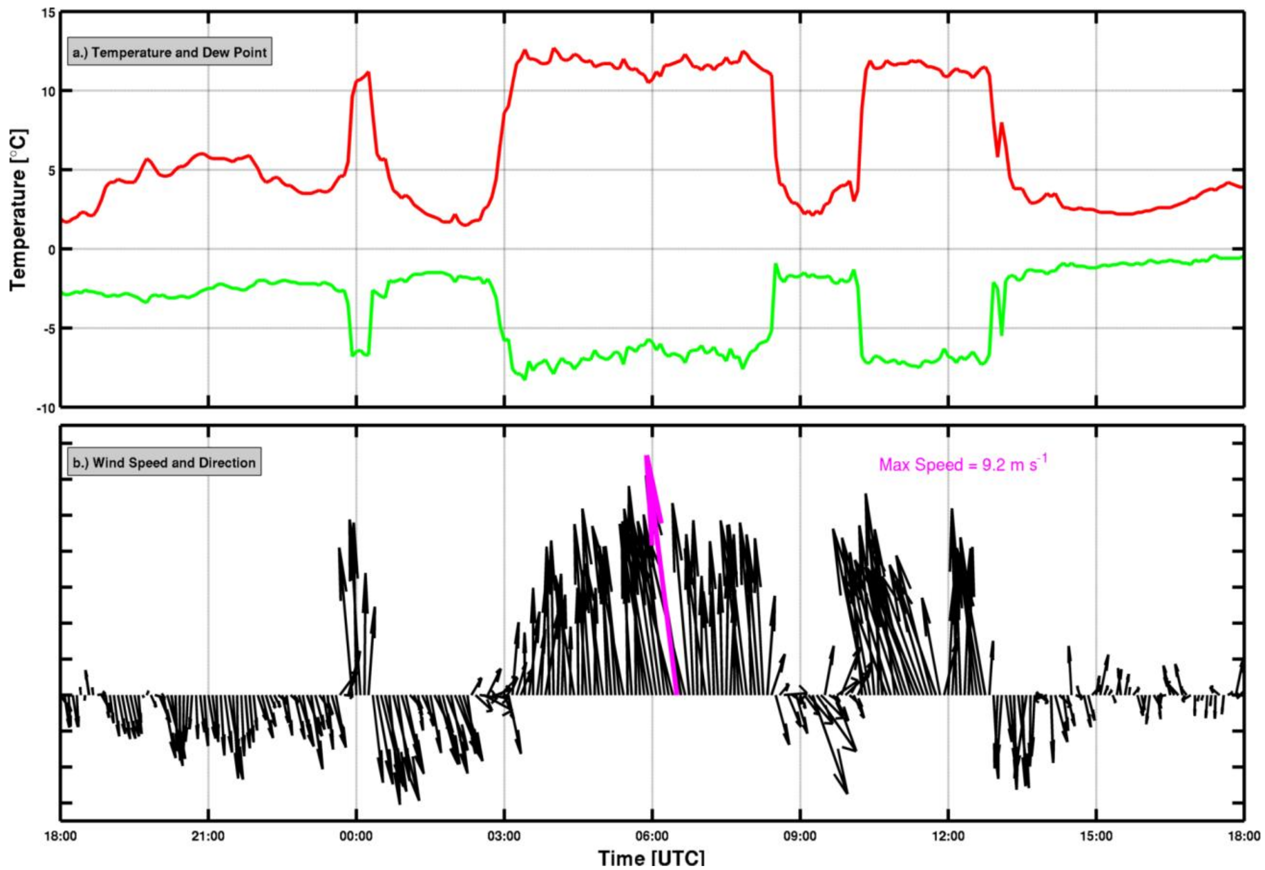

Fig. 5. Time series of (a) temperature (red line) and dew point temperature (green line) and (b) vector winds with the maximum speed shown in magenta for reference.

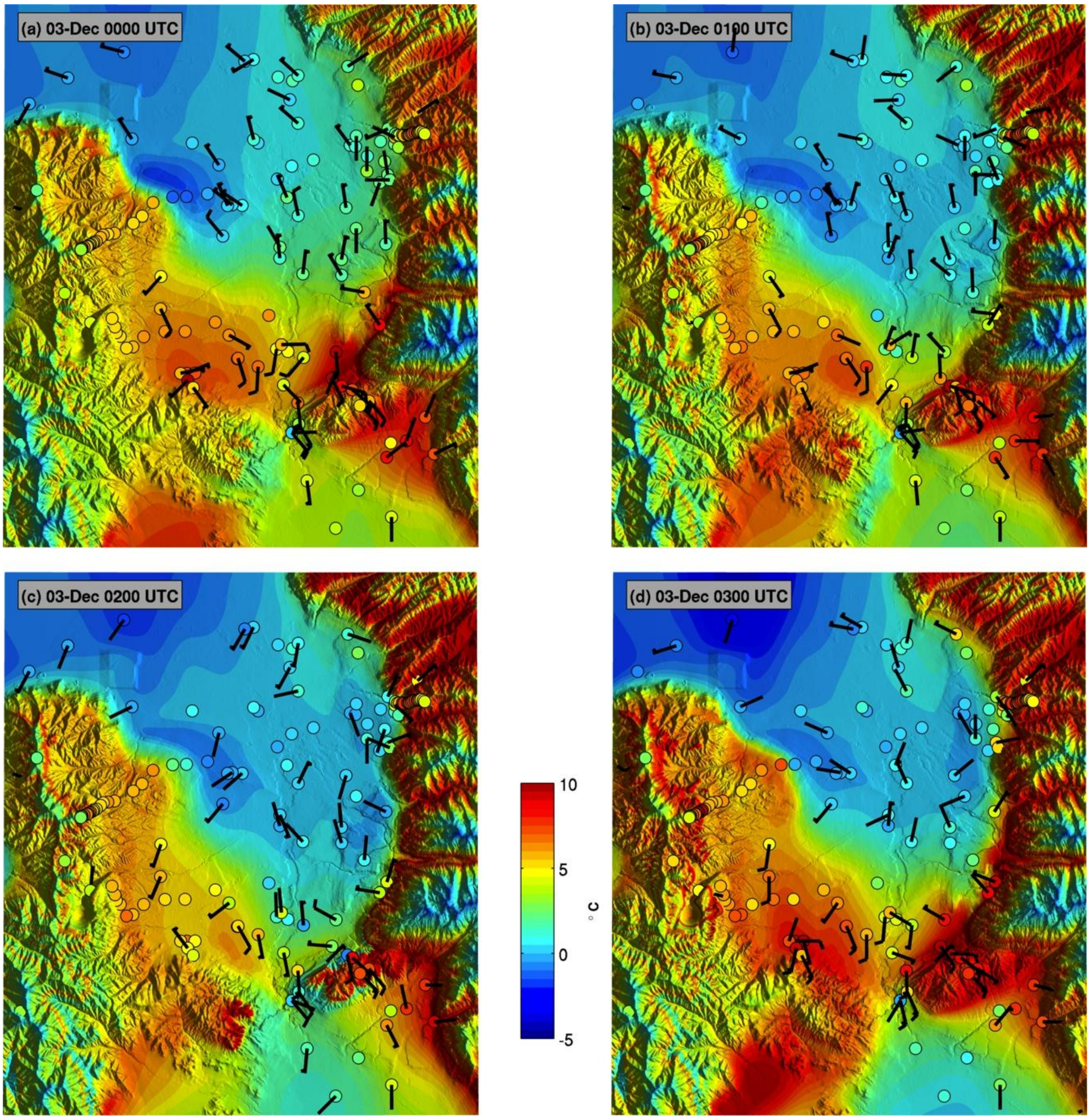

Fig 6. Hourly surface temperature analyses (colour shaded) from 0000-0300 UTC 3 December 2010. Surface temperature observations (filled circles shaded according to the scale) and vector wind (wind barbs in m/s where a full barb denotes 5 m/s).

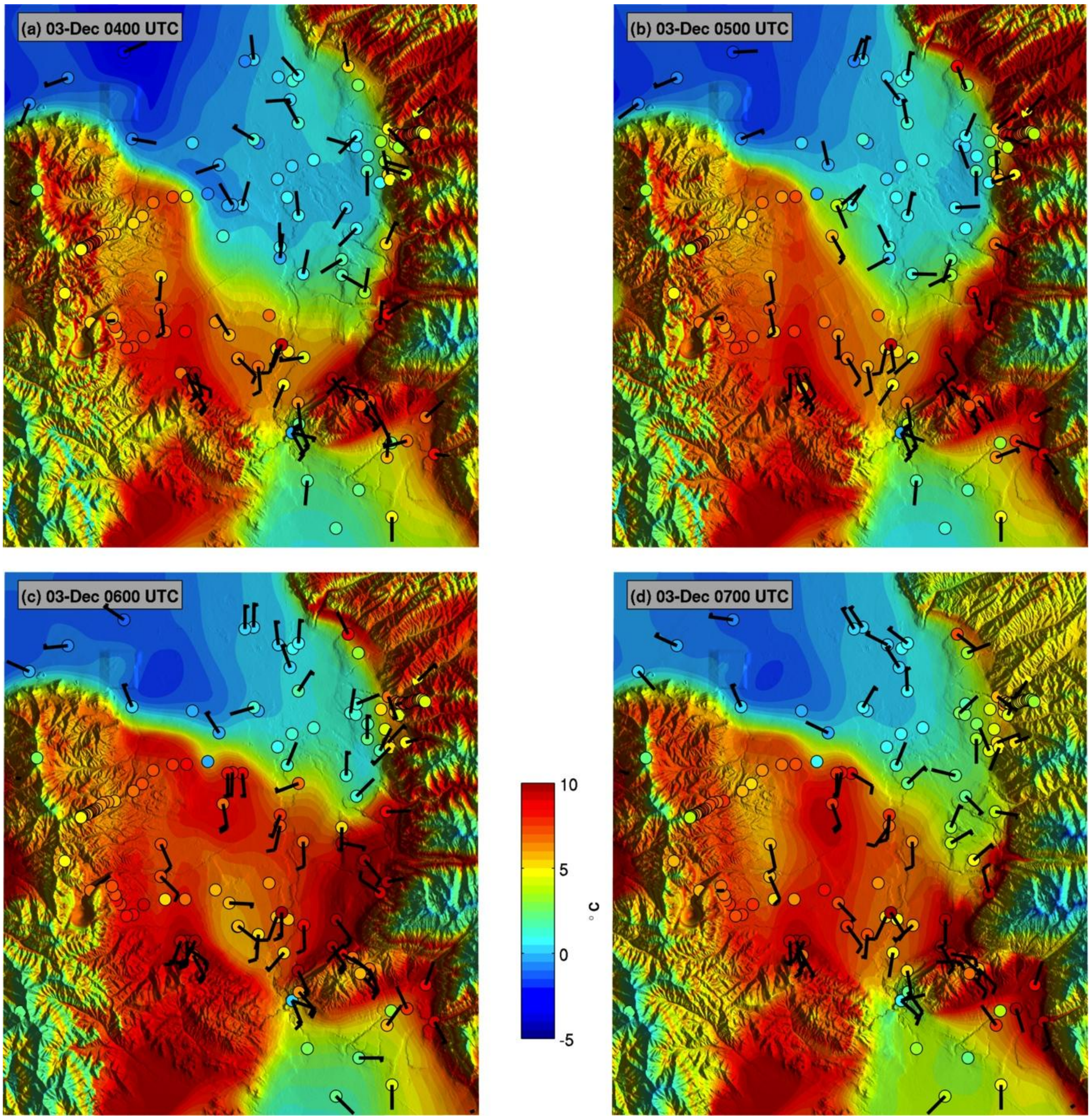

Fig 7. As in Fig. 6 except for 0400-0700 UTC 3 December.

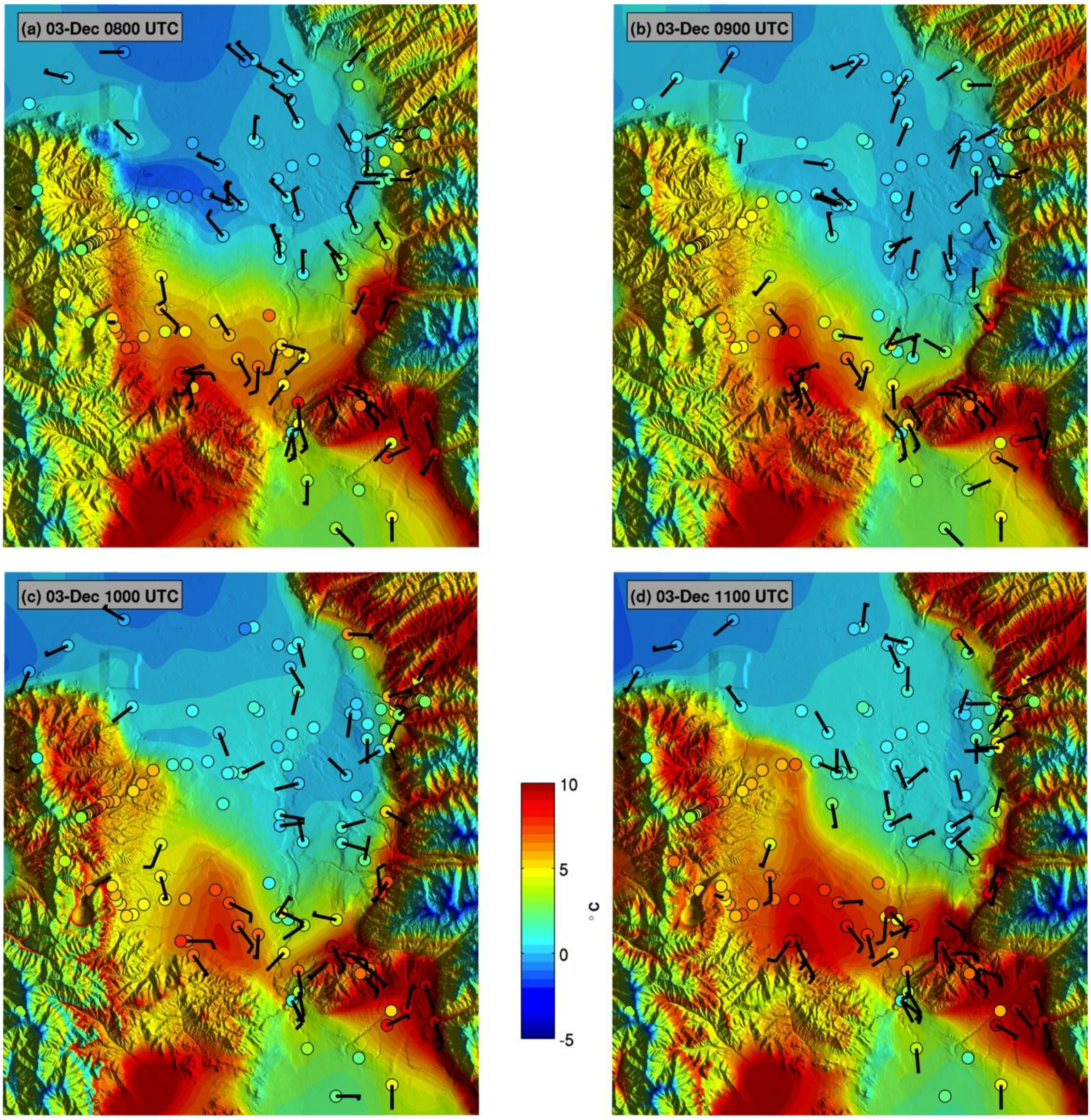

Fig. 8. As in Fig. 6 except for 0800-1100 UTC 3 December.

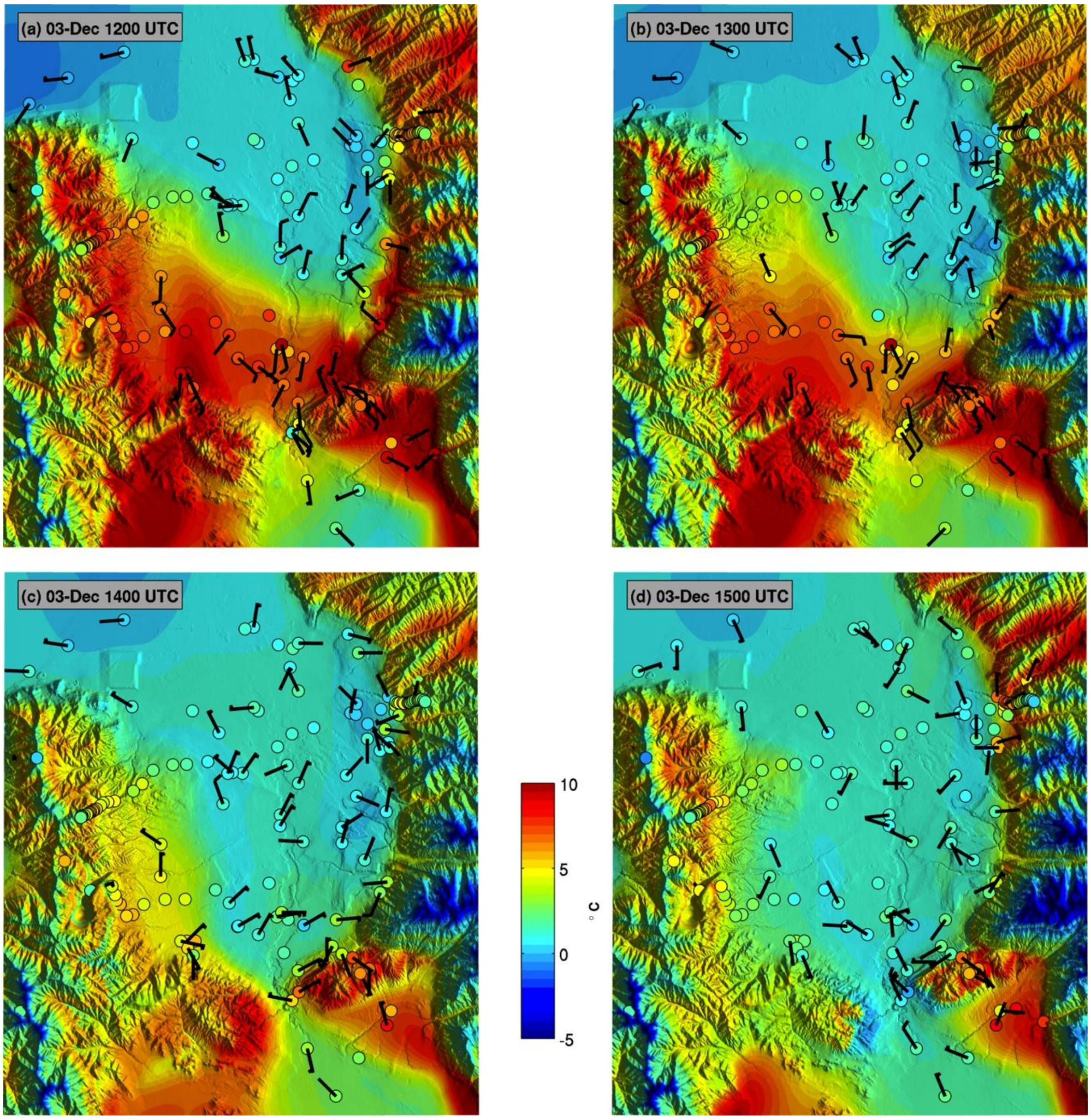

Fig 9. As in Fig. 6 except for 1200-1500 UTC 3 December.

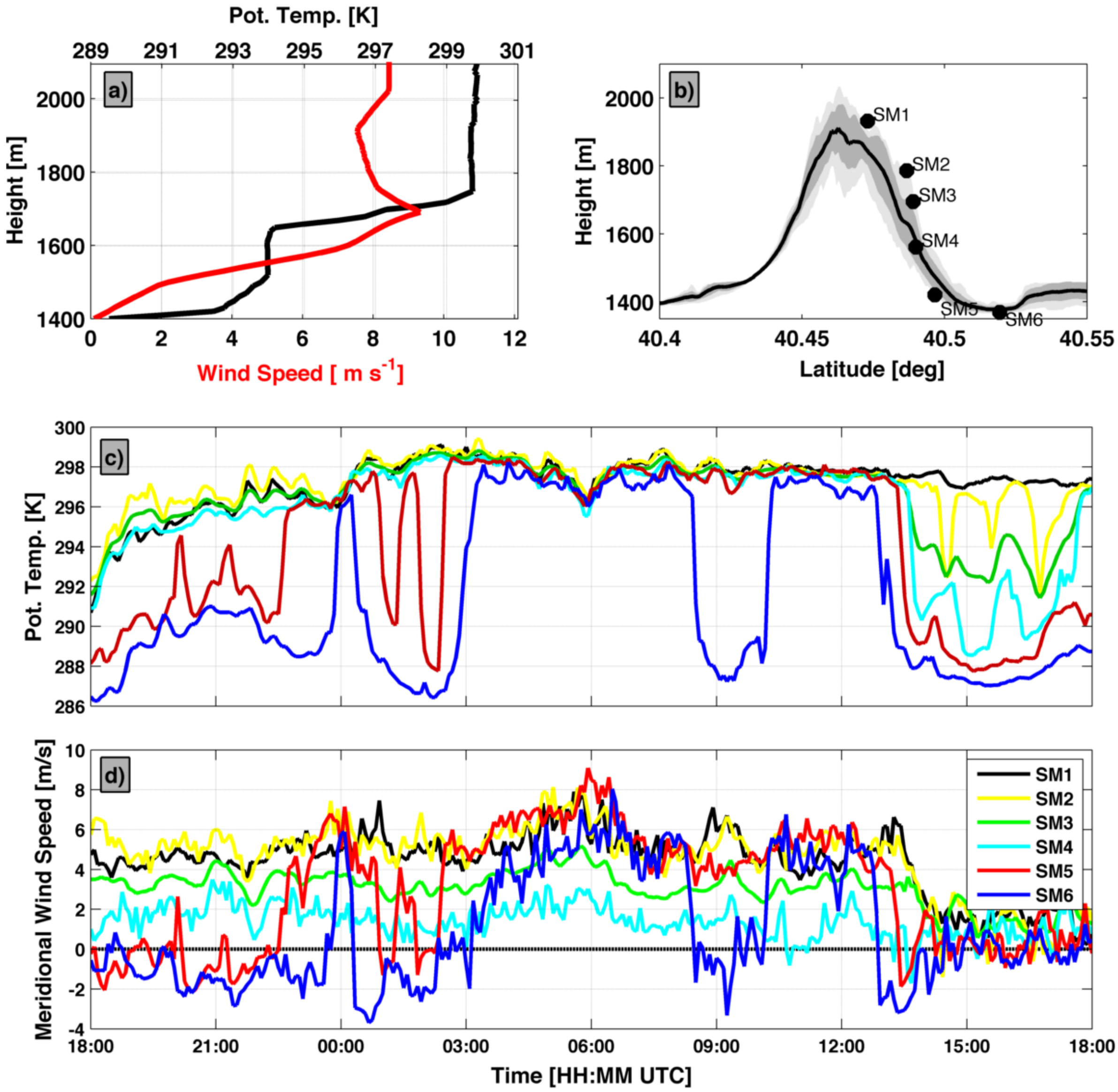

Fig. 10. Properties of the mountain wave forming over the Traverse Mountains. (a) Sounding upstream of the SLV at 0600 UTC 3 December showing potential temperature (black) and meridional wind (red). (b) Traverse Mountain cross-section showing station locations and the terrain variability (shading). (c) Potential temperature and (d) meridional wind time series for each of the 6 SM stations.

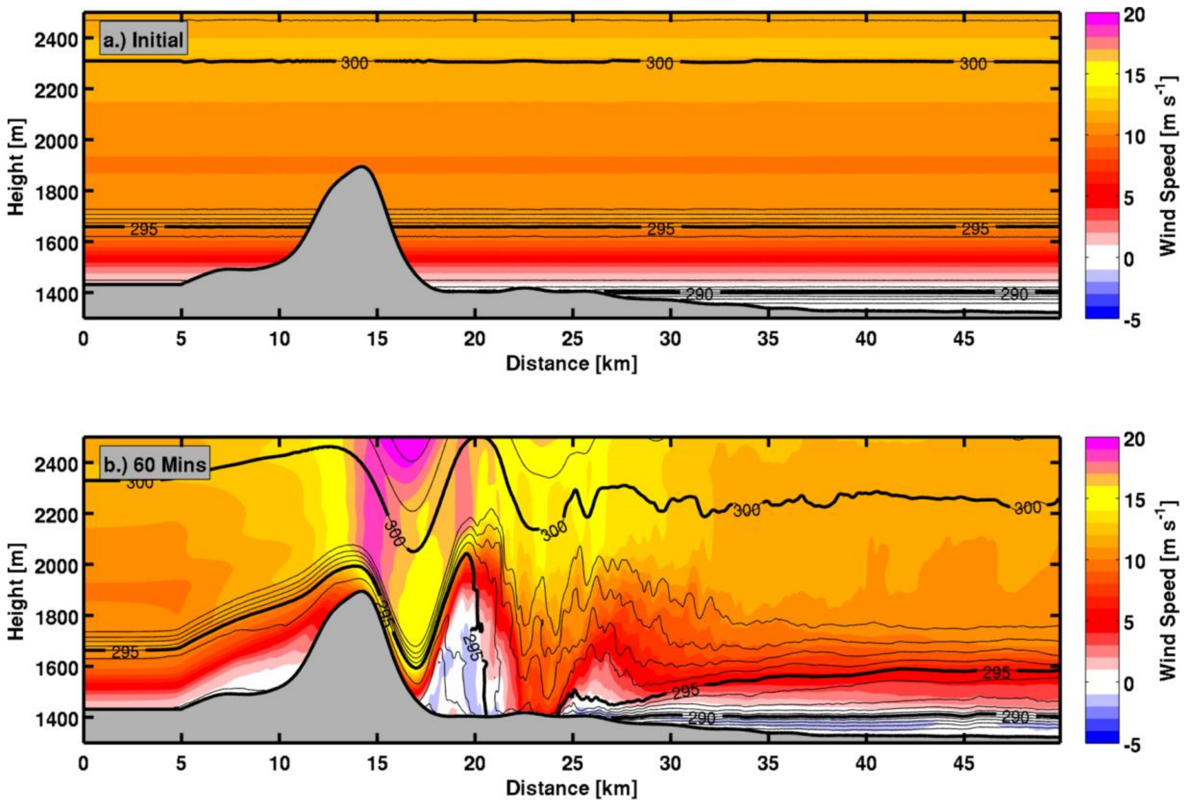

Fig. 11. Large-Eddy Simulation of a mountain wave disrupting the two-layered CAP. Panels show wind speed (colours) and potential temperature (contours, bold every 5 K) at (a) the initialization and (b) after 1-h of simulation.

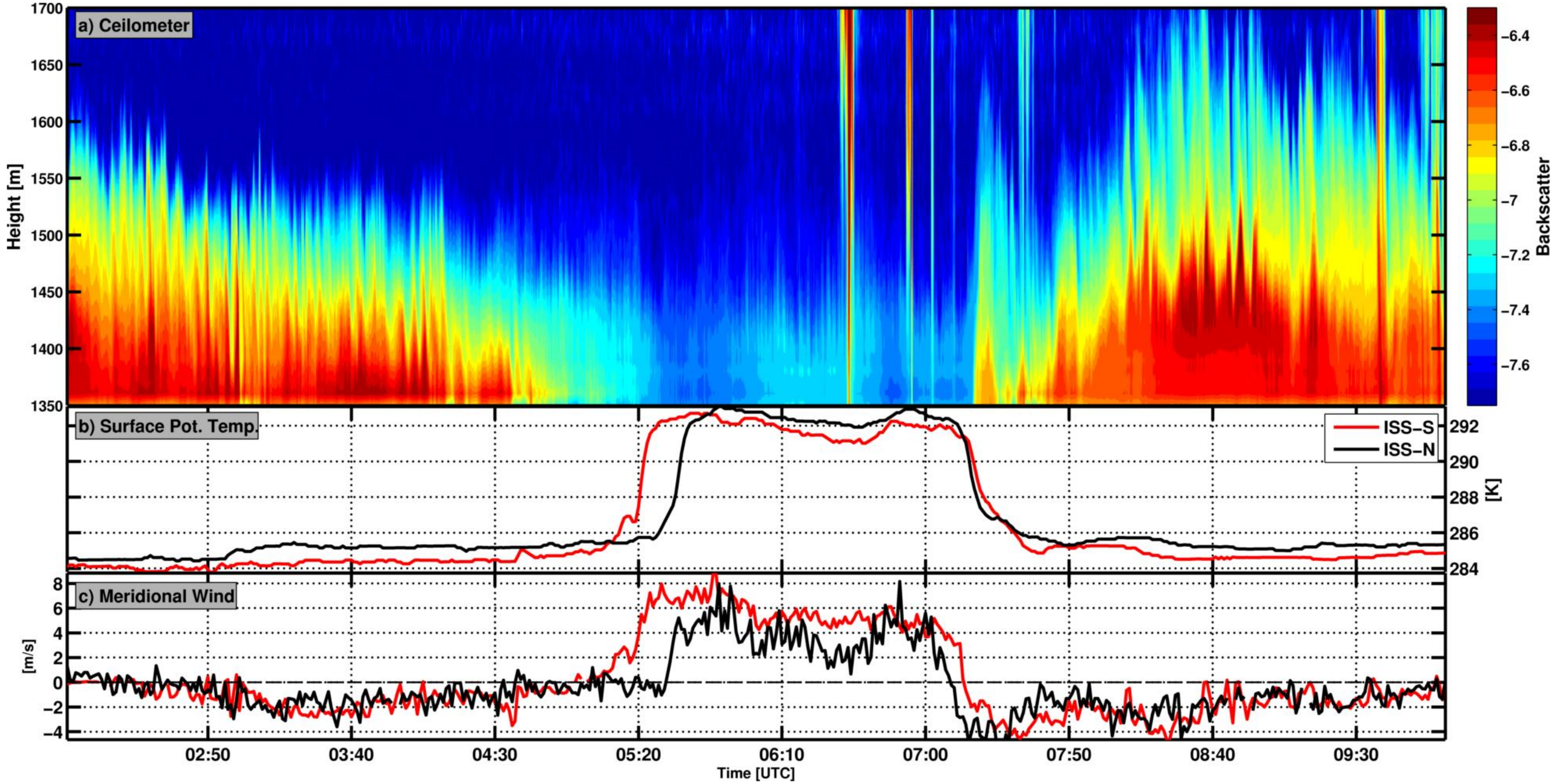

Fig. 12. Time series data during the warm and cold frontal passages at ISS-S and ISS-N on 3 December 2010. (a) Laser ceilometer backscatter, (b) potential temperature, and (c) meridional wind.

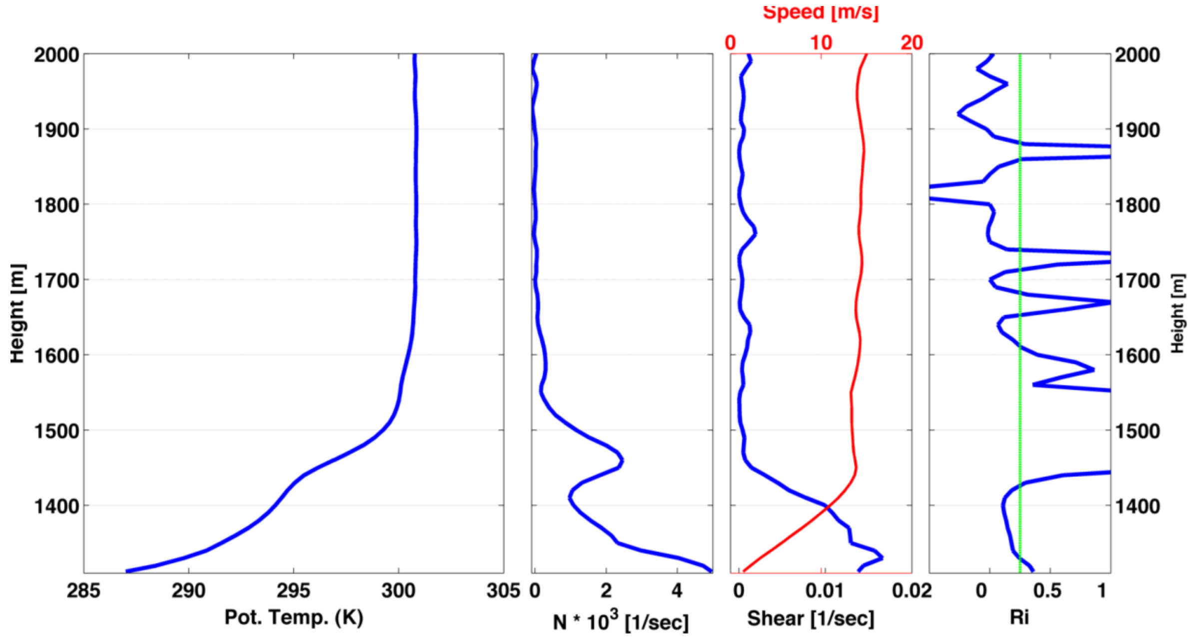

Fig. 13. Sounding from ISS-S at 05:14 UTC 3 December. (a) Potential temperature, (b) Brunt-Vaisala frequency, (c) wind speed and wind shear, and (d) the gradient Richardson number with the critical value marked in green.

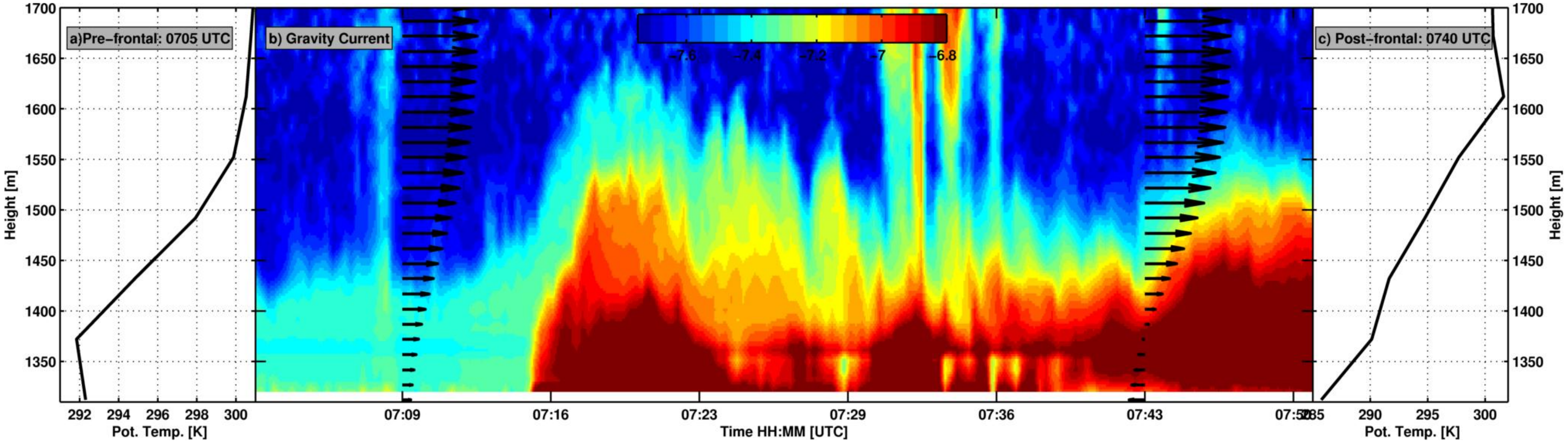

Fig. 14. Detail of the gravity current passage at ISS-S. (a) Prefrontal potential temperature profile at 0705 UTC, (b) ceilometer backscatter and meridional wind profiles from the radar wind profiler, and (c) post-frontal potential temperature profile at 0740 UTC. Profile data is retrieved from the time-height data set.

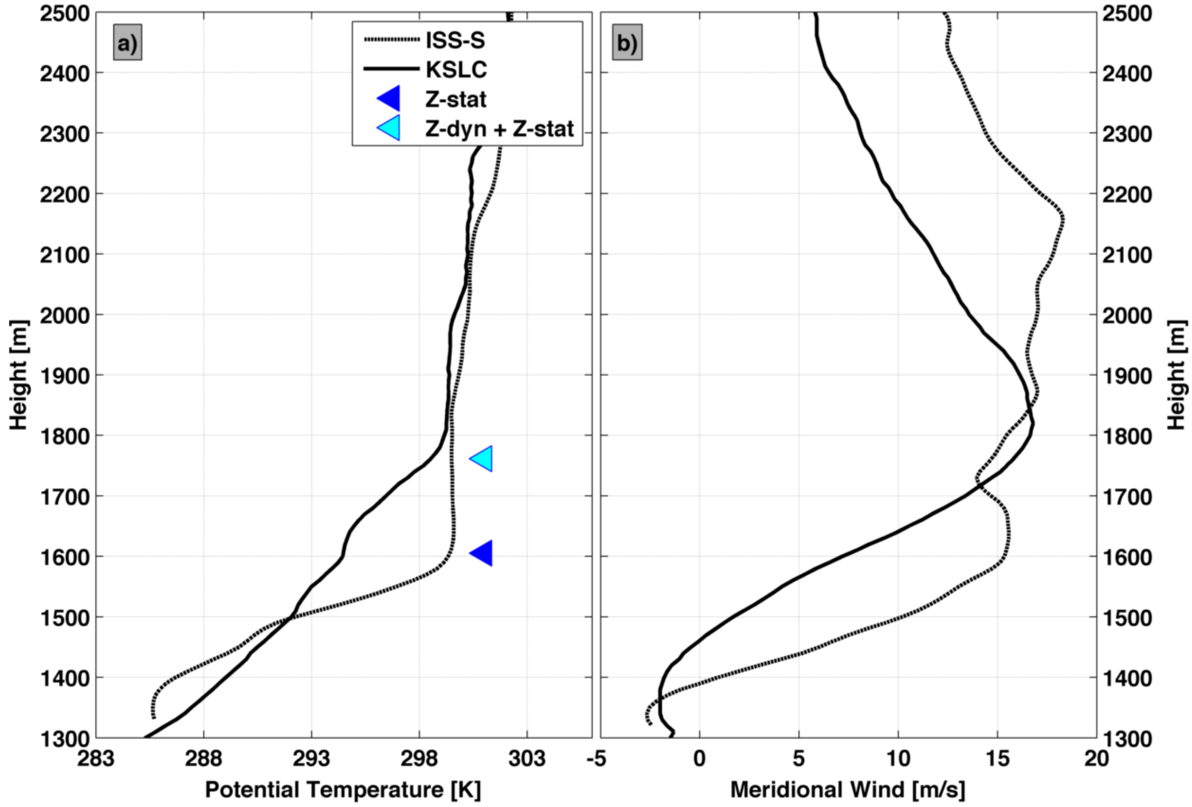

Fig. 15. Vertical profiles of (a) potential temperature and (b) meridional wind launched at 1115 UTC at KSLC (solid lines) and ISS-S (dashed lines). The shaded triangles are estimates of the CAP depth at KSLC from the static and dynamic + static forcing.

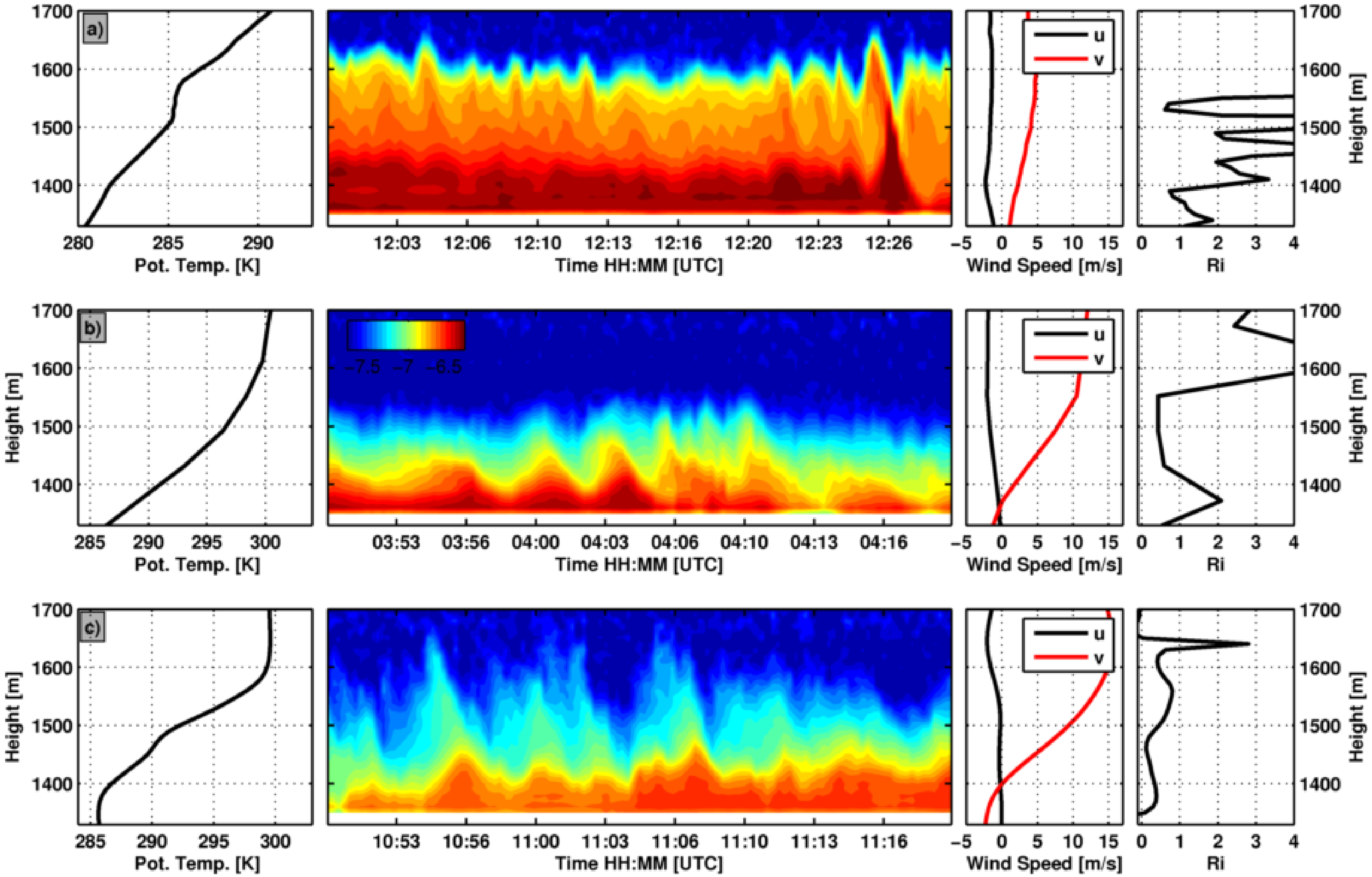

Fig. 16. Kelvin Helmholtz waves at: (a) ~1200 UTC 2 December, (b) ~0400 UTC 3 December, and (c) ~1100 UTC 3 December. First column: potential temperature. Second column: aerosol backscatter. Third column: wind speed. Last column: gradient Richardson number.

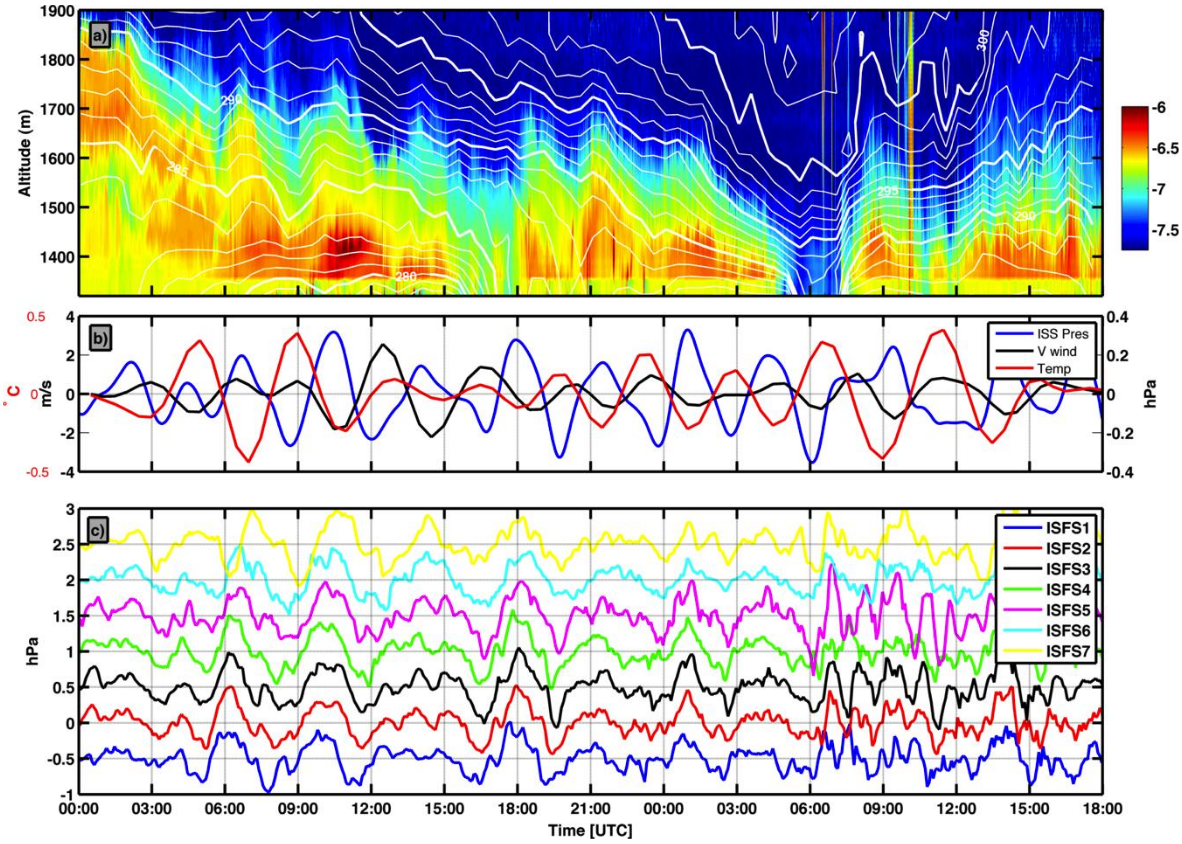

Fig. 17. Conditions at ISS-S from 0000 UTC 2 December to 1800 3 December of: (a) aerosol backscatter (shaded) with potential temperature (contours), (b) Band-pass filtered perturbations of ISS-S surface pressure (blue), and 1500-1800 m mean meridional wind (black), and potential temperature (red). (c) High-pass filtered surface pressure perturbations at each ISFS site. Curves are offset by 0.5 hPa.

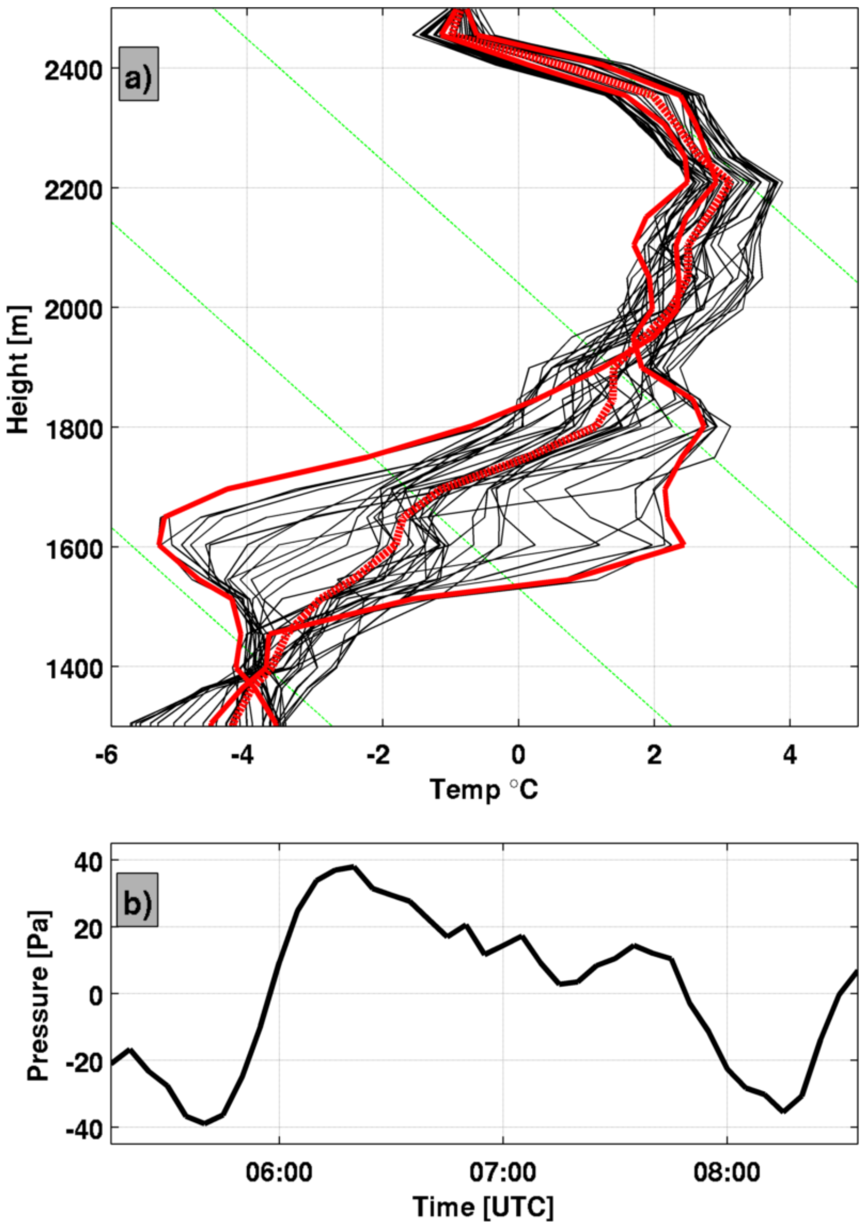

Fig. 18. (a) Harker's Ridge temperature profiles every 5 minutes between 0525 and 0830 UTC during the passage of one BSIW. Red lines indicate the mean and extreme profiles and the dashed green lines are adiabats. (b) The surface pressure perturbation computed from temperature anomalies.

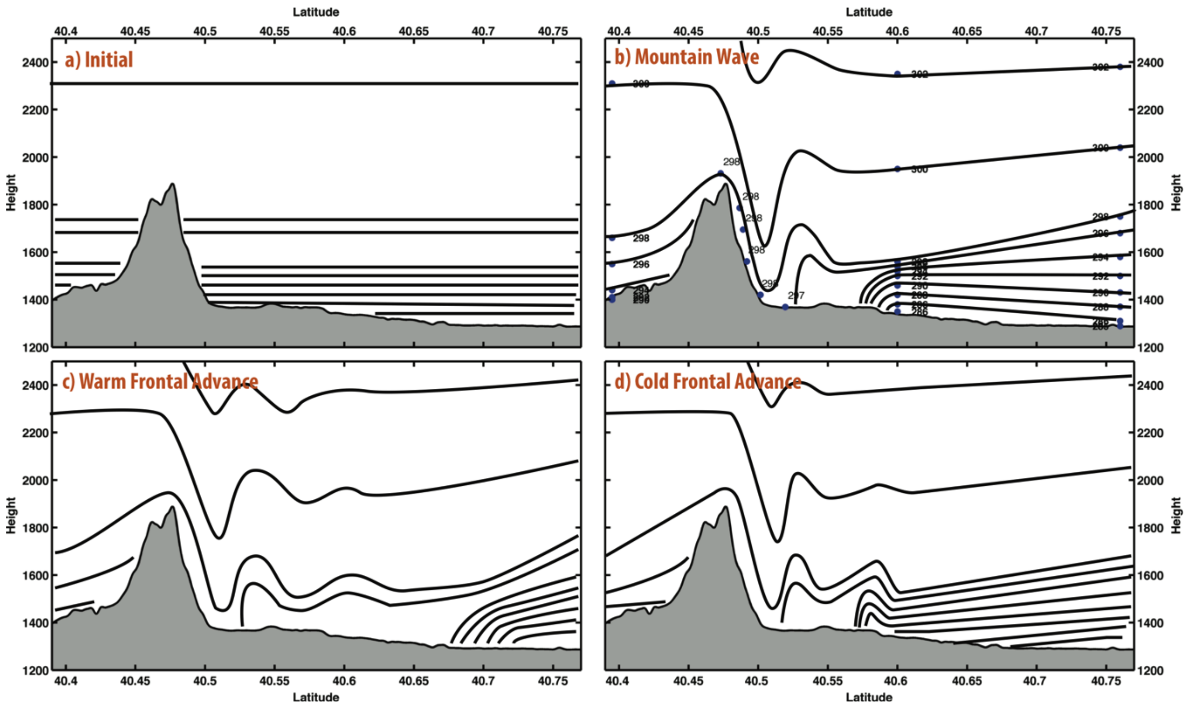

Fig. 19. Schematic of CAP displacement. Stages described in the text.